# Imaging the distribution of transient viscosity following the 2016 Mw 7.1 Kumamoto earthquake

James D. P. Moore[1*], Hang Yu[2], Chi-Hsien Tang[3], Teng Wang[1], Sylvain Barbot[1*], Dongju Peng[1], Sagar Masuti[1], Justin Dauwels[2], Ya-Ju Hsu[3], Valère Lambert[1], Priyamvada Nanjundiah[1], Shengji Wei[1], Eric Lindsey[1], Lujia Feng[1] and Bunichiro Shibazaki[4].

[1]Earth Observatory of Singapore, Nanyang Technological University
[2]School of Electrical & Electronic Engineering, Nanyang Technological University
[3]Institute of Earth Sciences Academia Sinica, Taipei, Taiwan
[4]International Institute of Seismology and Earthquake Engineering, Building Research Institute, Japan
[*]To whom correspondence should be addressed; E-mail: earth@jamesdpmoore.com and sbarbot@ntu.edu.sg.

The deformation of mantle and crustal rocks in response to stress plays a crucial role in the distribution of seismic and volcanic hazards, controlling tectonic processes ranging from continental drift to earthquake triggering. However, the spatial variation of these dynamic properties is poorly understood as they are difficult to measure. We exploit the large stress perturbation incurred by the 2016 earthquake sequence in Kumamoto, Japan to directly image localized and distributed deformation. The earthquakes illuminated distinct regions of low effective viscosity in the lower crust, notably beneath the Mt Aso and Mt Kuju volcanos, surrounded by larger scale variations of viscosity across the back-arc. This study demonstrates a new potential for geodesy to directly probe rock rheology in situ across many spatial and temporal scales.

Crustal dynamics involves the nonlinear interactions of faulting, ductile flow, and fluid migration, entwined with a complex thermal and metamorphic history. In addition to elastic deformation in the crust, there are a number of anelastic deformation mechanisms, including slip on faults in earthquakes and off-fault distributed ductile flow. The spatial distribution of the viscous properties in particular are poorly known, yet they play a key role in plate tectonics [1] and earthquake triggering [2,3,4]. Geodetic observation and modelling illuminates a range of these anelastic mechanisms activated in the aftermath of earthquakes. In particular, faults continue creeping aseismically for several months after the mainshock (afterslip), with accelerated ductile flow at depth [5] and in the surrounding rocks. Many studies exploit space geodetic data to infer the viscous properties of the lower crust and mantle using sophisticated models of stress relaxation [6,7,8,9], revealing the nonlinear rheology of rocks and transient creep, while other studies employ proxies such as magnetotellurics [10]. Despite these efforts, our knowledge of the spatial distribution of anelastic properties and mechanical strength variations remains limited. This is due in part to the complexity of distinguishing between deformation mechanisms, which often produce similar surface deformation [11]. Additionally, kinematic models of crustal deformation have hitherto been limited to slip on faults, hindering inference about the kinematics and rheology of distributed deformation. We address this by treating the kinematics of fault slip and distributed deformation concurrently, utilizing novel Green's functions for distributed deformation [12].

We exploited the spatial and temporal resolution of Interferometric Synthetic Aperture Radar (InSAR) observations from the European Sentinel-1A and Japanese ALOS-2 satellites combined with dense Global Positioning System (GPS) measurements from the Japanese GEONET to directly image the localized and distributed deformation that followed the 2016 Kumamoto, Japan earthquake sequence (Fig. 1). We assimilate InSAR line-of-sight (LOS) and GPS displacement time series spanning before, during, and after the Kumamoto earthquakes to describe the details of coseismic slip, afterslip, and lower-crustal ductile flow. We found large variations of viscosities across Kyushu, primarily due to thermal fluctuations in the lower crust related to the volcanic arc.

The Kumamoto earthquake sequence began on 14th April 2016 at 21:26 JST when a Mw 6.1 foreshock struck the southern Japanese island of Kyushu [13]. It was closely followed on 16th April 2016 at 01:25 JST by the Mw 7.0 mainshock, which resulted in the loss of 72 lives [14] and widespread structural damage due to the intense ground shaking. These earthquakes and their aftershocks occurred on the Futagawa and Hinagu fault zones (Fig. 1), with a measured right-lateral strike-slip surface offset of 2m [15] and a coseismic rupture front that terminated beneath Mt Aso [16]. The Futagawa and Hinagu fault zones make up the westward extension of the Median Tectonic Line and take up 25% of the margin parallel component of deformation at the Ryukyu trench [17]. In addition, there is N-S extension within the Beppu–Shimabara Graben [18] and arc volcanism associated with the Ryukyu trench coincident with these structures (Fig. 1).

We inferred the kinematics of the earthquake sequence by assimilation of GPS coseismic offsets and InSAR data, using a combination of ascending and descending orbits. We invert ALOS-2 InSAR images and GEONET GPS data to obtain the total coseismic rupture of both the foreshock and the mainshock [19]. The co-seismic slip inversion shows predominantly right lateral strike-slip motion, a peak slip of 5m and surface rupture of approximately 2m, with each earthquake occurring on separate fault segments (Fig. 1). We also find a normal-slip component on the Futagawa fault. These results are in close agreement both with those found using seismic waveform inversion [20] and the measured surface rupture [15]. The two earthquakes induced a cumulative coseismic stress change of the order of 1 MPa in the lower crust, large enough to trigger accelerated viscoelastic flow.

We extracted the 91-day postseismic deformation from the GPS time series for 321 stations [19], revealing a coherent velocity field at Earth's surface (Fig. 1), presumably caused by a combination of transient distributed deformation and afterslip. The greatest magnitude velocities are generally found in the northern half of Kyushu. In the near field there are a number of large amplitude, short wavelength features, indicative of local aftershocks and shallow aseismic afterslip. A few GPS stations exhibit anomalous velocities, most notably the one situated next to Tsurumi volcano in the Beppu–Shimabara Graben, moving in the opposite sense to its neighbours, with the largest magnitude of any station. A Mw5.7 aftershock near Tsurumi volcano triggered 30 seconds after the mainshock is responsible for the observed anomalous velocity, as we clearly see a stepwise eastward offset in the GPS time series. The GPS velocity field may also be affected by the aseismic motion of small cracks near the surface [21]. Additionally, we unwrapped the Sentinel-1A InSAR frames and used the GPS stations to correct orbital aberrations, providing absolute LOS velocities.

The kinematics of the postseismic deformation following the Kumamoto earthquake sequence can be largely reduced to localized slip on faults and distributed strain in finite volumes [22,23] (Figs. 2, S4), corresponding to afterslip on the Futagawa and Hinagu fault zones and ductile flow in the lower crust respectively. We divided up the Futagawa and Hinagu faults into 2x2 km square patches [24], and the lower crust into 15x15x7.5 km cuboid volumes [12]. We aligned the strike of the strain volumes with the average fault strike and located them in the bottom 15 km of the plate beneath Kyushu using Litho 1.0 for the Moho depth [25]. This results in an allowed anelastic deformable region with depth range between 20 km and 40 km. In addition, we include 6 cuboid strain volumes (30x125x30km) in the mantle wedge, located between the Moho and the at a depth of 50-80 km.

We looked for the linear combination of strain rate in finite volumes and slip velocity on the Futagawa and Hinagu faults that best explained the instantaneous postseismic velocities in the GPS and InSAR data. Ductile flow in each of the deformable volumes comprises six independent directions of strain (Fig. S4) and faulting requires two directions of slip, giving rise to a large number of free parameters. To avoid over-fitting the data, we regularized the problem by penalizing isotropic strain rates and directions that are orthogonal to the induced coseismic stress change, and by minimizing the postseismic stress change rate, a form of smoothing. Slip is also penalized in the coseismic region and in directions orthogonal to the forces induced by the coseismic rupture [19].

Even if the glut of free parameters from the deformable strain volumes and fault patches are reasonably well balanced by a wealth of observational data and additional constraints, inferring the spatial distribution of localized and distributed deformation at crustal depths represents a substantial challenge. We constructed an outlier-insensitive hierarchical Bayesian model [19] by incorporating all constraints into the priors. We then used a Monte-Carlo Markov Chain algorithm to sample from the posterior distribution of the slip and strain-rate parameters, and the constraint weights given the GPS and InSAR data, resulting in estimates of these parameters as well as their uncertainties. This allowed us to carefully balance overfitting the data with possibly significant outliers and drawing inferences as to the most likely cause of deformation beneath Kyushu.

We illustrate the robustness of our approach by carrying out a series of synthetic tests [19], including checkerboards (Fig. S6 and S7) and the recovery of forward models where we assumed uniform and spatially varying viscosity in the lower crust (Fig. S8, S9 and S10). To attempt to replicate the perils of using real data, we randomly introduced noise and large outliers into the displacement fields. The recovered models indicate that we can clearly differentiate between viscous flow and afterslip, though the viscoelastic flow is smoothed from the input. Perhaps unsurprisingly, the best resolution is obtained where we have both GPS and InSAR coverage, and the worst is located in the submarine regions. The smoothing of the recovered model is imposed to prevent overfitting the noise in the data or velocities due to sources not incorporated in the model. The synthetic tests also allow us to quantify the error associated with the recovered viscosities of 30%, or half an order of magnitude.

Our approach allows us to intrinsically disentangle the complex interactions between

afterslip and ductile flow and to describe their relative contributions to the surface velocities. We find shallow afterslip on the Hinagu fault, with a broader region of afterslip on the eastern end of the Futagawa fault (Fig. 2), with velocities in the range predicted by typical frictional parameters under this stress perturbation [26]. The strain rates in the lower crust broadly follow the independently obtained contours of coseismic stress change (Fig. 2), as expected for ductile flow, with distinct regions of high strain rate, most notably beneath the volcanic edifices of Mt Aso and Mt Kuju. Because of smoothing, the technique does not currently resolve differences between the top and bottom of the lower crust. The preferred model reproduces the observed InSAR data very closely, with 91% variance reduction (Fig. 3 and S11), and matches the GPS data reasonably closely, with 84% variance reduction. The far-field velocities are dominated by viscoelastic flow in the lower crust, with only a handful of near-field GPS stations and InSAR picking up the afterslip (Fig. 3). For this data set, the statistical algorithm has preferentially matched the InSAR observations above the GPS when balancing constraints and slight inconsistencies between the data sources, a known issue with joint inversions [27]. This is due to more significant errors associated with GPS, especially the vertical component which has a large scatter (RMS of 10mm or more) and is, in general, less suitable for use over this time period. In particular, we misfit some of the GPS stations and InSAR points located closest to the Futagawa fault, likely due to localized shallow deformation not included in our model such as surface cracks or poroelastic rebound.

The viscosity of rocks depends on many physical parameters including local stress, strain rate, temperature, water content, composition and degree of metamorphism, leading to tremendous uncertainties in the strength of the lower crust. We estimate the effective transient viscosity of the lower crust beneath Kyushu from the inferred kinematics using

$$\eta_{\text{eff}} = \frac{\tau}{\dot{\epsilon}}$$

where $\tau$ and $\dot{\epsilon}$ are the effective stress and strain rate in the first hours following the earthquake (Fig. 4 and S12), obtained from the second invariant of the respective tensors. We included the pre-earthquake stress assuming a steady-state uniform viscosity of $10^{19}$ Pa s at a background strain rate of $10^{-15}$ $s^{-1}$ (0.03 μstrains/yr). We obtain effective viscosities in the range between $5\times10^{16}$ and $10^{19}$ Pa s, with the lowest viscosity beneath Mt Aso and Mt Kuju, in reasonable agreement to that found in another volcanic arc, beneath Santorini Volcano, Greece due to thermal activation [28,29] and commensurate with predictions for transient creep of a thermally activated non-linear rheology [6]. A similar low viscosity region is not found beneath Mt Unzen which, unlike the other volcanoes is related to the opening of the Okinawa trench. The highest values are controlled by our assumptions for pre-stress. The low viscosities we recovered require an elevated geothermal gradient and also hint at the existence of melt pockets in the crust beneath these volcanos. This low viscosity region would also damp the rupture propogation and explain why the coseismic rupture terminated here. The large anelastic, predominantly normal, strain rate beneath Mt Aso may also have helped induce the eruption on 8th October 2016. The broader regions of low viscosity follow the stress contour, compatible with activation of dislocation creep or transient creep. We interpret the low transient viscosities as the result of a combination of steady-state and transient creep mechanisms. The low effective viscosities in the northern

quadrant correspond to a large quaternary plutonic body associated with a significant heat flow anomaly [30]. We also find little deformation within the mantle wedge (~10 μstrain/yr), which would likely require a larger stress perturbation, such as the one created by the $M_w$ 8.6 Indian Ocean [6] or $M_w$ 9.0 Tōhoku earthquakes [7].

The postseismic deformation following the Kumamoto earthquake sequence brings insights into the distribution of brittle and ductile crustal processes beneath Kyushu, illuminating low transient effective viscosities in the lower crust, and thermally activated deformation beneath volcanic edifices. This provides a benchmark for the background variation in mechanical strength at a volcanic arc. The methodology introduced in this study reveals a new potential for geodesy to shed light on the mechanics of distributed deformation and brings us one step closer to building a rheological model of the lithosphere–asthenosphere system.

**References**


1. S. Zhong, M. Gurnis, Mantle convection with plates and mobile, faulted plate margins. *Science,* ***267***(5199), 838 (1995).
2. A. M. Freed, J. Lin, Delayed triggering of the 1999 Hector Mine earthquake by viscoelastic stress transfer. *Nature*, ***411***(6834), 180–183 (2001).
3. A. Ziv, A. M. Rubin, Static stress transfer and earthquake triggering: No lower threshold in sight? *J. Geophys. Res.,* ***105***(B6), 13631–13642 (2000).
4. J. Gomberg, N. M. Beeler, M. L. Blanpied, P. Bodin, Earthquake triggering by transient and static deformations. *J. Geophys. Res.,* ***103***(B10), 24411–24426 (1998).
5. R. Bürgmann, G. Dresen, Rheology of the Lower Crust and Upper Mantle: Evidence from Rock Mechanics, Geodesy, and Field Observations. *Annual Review of Earth and Planetary Sciences*, ***36***(1), 531–567 (2008).
6. S. Masuti, S. D. Barbot, S. Karato, L. Feng, P. Banerjee, Upper-mantle water stratification inferred from observations of the 2012 Indian Ocean earthquake. *Nature*, **538**, 373-377 (2016).
7. Sun, T., K. Wang, T. Iinuma, R. Hino, J. He, H. Fujimoto, M. Kido, Y. Osada, S. Miura, Y. Ohta, Y. Hu, Prevalence of viscoelastic relaxation after the 2011 Tohoku-oki earthquake. *Nature,* **514**, 84-87 (2014).
8. B. Rousset, S. D. Barbot, J. Avouac, Y. Hsu, Postseismic deformation following the 1999 Chi-Chi earthquake, Taiwan: Implication for lower-crust rheology. *Journal of Geophysical Research: Solid Earth,* **117**.B12 (2012).
9. T. Yamasaki, T. J. Wright, G. A. Houseman, Weak ductile shear zone beneath a major strike-slip fault: Inferences from earthquake cycle model constrained by geodetic observations of the western North Anatolian Fault Zone. *J. Geophys. Res. Solid Earth,* **119**, 3678–3699 (2014).
10. L. Liu and D. Hasterok, High-resolution lithosphere viscosity and dynamics revealed by magnetotelluric imaging. *Science*, **353**(6307), 1515 (2016).
11. C. Rollins, S. D. Barbot, J. Avouac, Postseismic deformation following the 2010 Mw 7.2 El Mayor-Cucapah earthquake: Observations, kinematic inversions, and dynamic models. *Pure and Applied Geophysics* **172.5**: 1305-1358 (2015).

12. S. D. Barbot, J. D. P. Moore, V. Lambert, Displacements and Stress Associated with Distributed Anelastic Deformation in a Half Space. *Bull. Seismol. Soc. Am.* **107**(2), 10.1785/0120160237 (2017),
13. A. Kato, J. Fukuda, S. Nakagawa, K. Obara, Foreshock migration preceding the 2016 Mw 7.0 Kumamoto earthquake, Japan. *Geophys. Res. Lett.,* ***43***, (2016).
14. The Japan Times, Kumamoto marks fourth month since temblor left 72 dead, 16th August 2016 http://www.japantimes.co.jp/news/2016/08/16/national/kumamoto-set-mark-fourth-month-since-temblor-left-72-dead/
15. K. Okumura, Earthquake Geology of the April 14 and 16, 2016 Kumamoto Earthquakes. Report for the University of Hiroshima (2016; http://home.hiroshima-u.ac.jp/kojiok/kumamoto2016KOreport2.pdf).
16. A. Lin, T. Satsukawa, M. Wang, Z. Mohammadi Asl, R. Fueta, F. Nakajima, Coseismic rupturing stopped by Aso volcano during the 2016 Mw 7.1 Kumamoto earthquake, Japan. *Science* 10.1126/science.aah4629 (2016).
17. J. P. Loveless, B. J. Meade, Geodetic imaging of plate motions, slip rates, and partitioning of deformation in Japan. *J. Geophys. Res.,* **115**, B02410 (2010).
18. Tada, T., Spreading of the Okinawa trough and its relation to the crustal deformation in the Kyushu, *Zisin*, **37**, 3, 407-416, (1984).
19. Materials and methods are available as supplementary materials on Science online.
20. K. Asano, T. Iwata, Source rupture processes of the foreshock and mainshock in the 2016 Kumamoto earthquake sequence estimated from the kinematic waveform inversion of strong motion data. *Earth, Planets and Space* **68**, 147 (2016).
21. S. Fujiwara, H. Yarai, T. Kobayashi, Y. Morishita, T. Nakano, B. Miyahara, H. Nakai, Y. Miura, H. Ueshiba, Y. Kakiage, H. Une, Small‐displacement linear surface ruptures of the 2016 Kumamoto earthquake sequence detected by ALOS‐2 SAR interferometry. *Earth, Planets and Space* **68**, 160 (2016).
22. V. Lambert, S. D. Barbot, Contribution of viscoelastic flow in earthquake cycles within the lithosphere-asthenosphere system. *Geophys. Res. Lett.,* **43**(19), 142–154 (2016).
23. A. Noda, M. Matsu'ura, Physics-based GPS data inversion to estimate three-dimensional elastic and inelastic strain fields. *Geophys. J. Int.* **182**, 513–530 (2010).
24. Y. Okada, Surface deformation due to shear and tensile faults in a half-space. *Bull. Seismol. Soc. Am.*, **75**, 1135–1154 (1985).
25. M.E. Pasyanos, T. G. Masters, G. Laske, Z. Ma, LITHO1.0: An updated crust and lithospheric model of the Earth. *J. Geophys. Res.*, **119**(3), 2153-2173, (2014).
26. N. Lapusta, S. D. Barbot, Models of earthquakes and aseismic slip based on laboratory-derived rate and state friction laws. *The Mechanics of Faulting: From Laboratory to Real Earthquakes*, 153-207 (2012).
27. G. J. Funning, Y. Fukahata, Y. Yagi, B. Parsons. A method for the joint inversion of geodetic and seismic waveform data using ABIC: application to the 1997 Manyi, Tibet, earthquake. *Geophys. J. Int.* **196** (3): 1564-1579 (2014).
28. M. M. Parks, J. D. P. Moore, X. Papanikolaou, J. Biggs, T. A. Mather, D. M. Pyle, C. Raptakis, D. Paradissis, A. Hooper, B. Parsons, P. Nomikou, From quiescence to unrest: 20 years of satellite geodetic measurements at Santorini volcano, Greece. *J. Geophys. Res. Solid Earth,* **120** 1309–1328 (2015).
29. A. B. Watts, P. Nomikou, J. D. P. Moore, M. M. Parks, M. Alexandri, Historical bathymetric charts and the evolution of Santorini submarine volcano, Greece. *Geochem. Geophys. Geosyst.,* **16**, 847–869 (2015).

30. A. Tanaka, M. Yamano, Y. Yano, M. Sasada, Geothermal gradient and heat flow data in and around Japan (I): Appraisal of heat flow from geothermal gradient data. *Earth Planets Space,* **56**, 1191–1194 (2004).
31. S. Barbot and Y. Hamiel and Y. Fialko (2008), Space geodetic investigation of the coseismic and postseismic deformation due to the 2003 Mw 7.2 Altai earthquake: Implications for the local lithospheric rheology, J. Geophys. Res., 113, B03403, 10.1029/2007JB005063.
32. S. Barbot and Y. Fialko and Y. Bock (2009), Postseismic Deformation due to the Mw 6.0 2004 Parkfield Earthquake: Stress-Driven Creep on a Fault with Spatially Variable Rate-and-State Friction Parameters, J. Geophys. Res., 114, B07405.
33. S. Barbot and P. Agram and M. De Michele (2013), Change of Apparent Segmentation of the San Andreas Fault Around Parkfield from Space Geodetic Observations Across Multiple Periods, J. Geophys. Res., 118, 12, 6311-6327.
34. Zumberge, J. F., Heflin, M. B., Jefferson, D. C., Watkins, M. M., and Webb, F. H. (1997). Precise point positioning for the efficient and robust analysis of GPS data from large networks. Journal of Geophysical Research: Solid Earth, 102(B3), 5005-5017.
35. Feng, L., E. M. Hill, P. Banerjee, I. Hermawan, L. L. H. Tsang, D. H. Natawidjaja, B.W. Suwargadi, and K. Sieh (2015), A unified GPS-based earthquake catalog for the Sumatran plate boundary between 2002 and 2013, J. Geophys. Res. Solid Earth, 120, 35663598, doi:10.1002/2014JB011661.
36. Sandwell, D., R. Mellors, X. Tong, M. Wei and P. Wessel (2011), Open radar interferometry software for mapping surface deformation, Eos Trans. AGU, 92(28), doi:10.1029/2011EO280002.
37. Chen, C. W. and H. A. Zebker (2000), Network approaches to two-dimensional phase un- wrapping: intractability and two new algorithms. J. Opt. Soc. Am. A 17, 401-414, doi: 10.1364/JOSAA.17.000401
38. Agram, P. and R. Jolivet, Variable resolution interferogram resampler - User Guide (2012), http://earthdef.caltech.edu
39. Simons, M., Y. Fialko and L. Rivera (2002), Coseismic Deformation from the 1999 Mw 7.1 Hector Mine, California, Earthquake as Inferred from InSAR and GPS Observations. Bull. Seism. Soc. Am., 92, 1390-1402, doi:10.1785/0120000933.
40. Ji, C., Wald, D.J., Helmberger, D.V., 2002. Source description of the 1999 Hector Mine, Califor- nia, earthquake, part I: Wavelet domain inversion theory and resolution analysis. Bull. Seism. Soc. Am. 92, 1192-1207.
41. Wang, T., S. Jonsson, and R. Hanssen (2014), Improved SAR Image Coregistration Using Pixel-Offset Series, IEEE Geoscience and Remote Sensing Letters, 11(9), 14651469, doi:10.1109/LGRS.2013.2295429.
42. Schmid, R., Dach, R., Collilieux, X., J¨aggi, A., Schmitz, M., and Dilssner, F. (2016). Absolute IGS antenna phase center model igs08. atx: status and potential improvements. J. Geodesy, 90(4), 343-364.
43. Boehm, J., Werl, B., and Schuh, H. (2006). Troposphere mapping functions for GPS and very long baseline interferometry from European Centre for Medium?Range Weather Forecasts op- erational analysis data. J. Geophys. Res., 111(B2).
44. Altamimi, Z., Collilieux, X., and M´etivier, L. (2011). ITRF2008: an improved solution of the international terrestrial reference frame. Journal of Geodesy, 85(8), 457-473.

45. M. Tipping, Sparse Bayesian learning and the relevance vector machine, *J. Mach. Learn. Res.*, vol. 1, pp. 211-244, 2001.
46. L. Tierney, “Exploring posterior distributions using Markov chains,” in *Computer Science and Statistics: Proc 24rd Symp. Interface (ed. E. Keramidas)*, pp. 563-570. Fairfax Station: Interface Foundation.

## Acknowledgments

This research was supported by the National Research Foundation of Singapore under the NRF Fellowship scheme (National Research Fellow Awards NRF-NRFF2013-04) and by the Earth Observatory of Singapore, the National Research Foundation, and the Singapore Ministry of Education (Tier 2 project ARC5/14) under the Research Centres of Excellence initiative. We would also like to thank Yoshihiro Ito for supporting access to the GEONET data. Data used in this study is stored at the Earth Observatory of Singapore and is freely available upon request.

## Supplementary Material

Materials and Methods
Supplementary Text
Figures S1 to S12
References 31-46

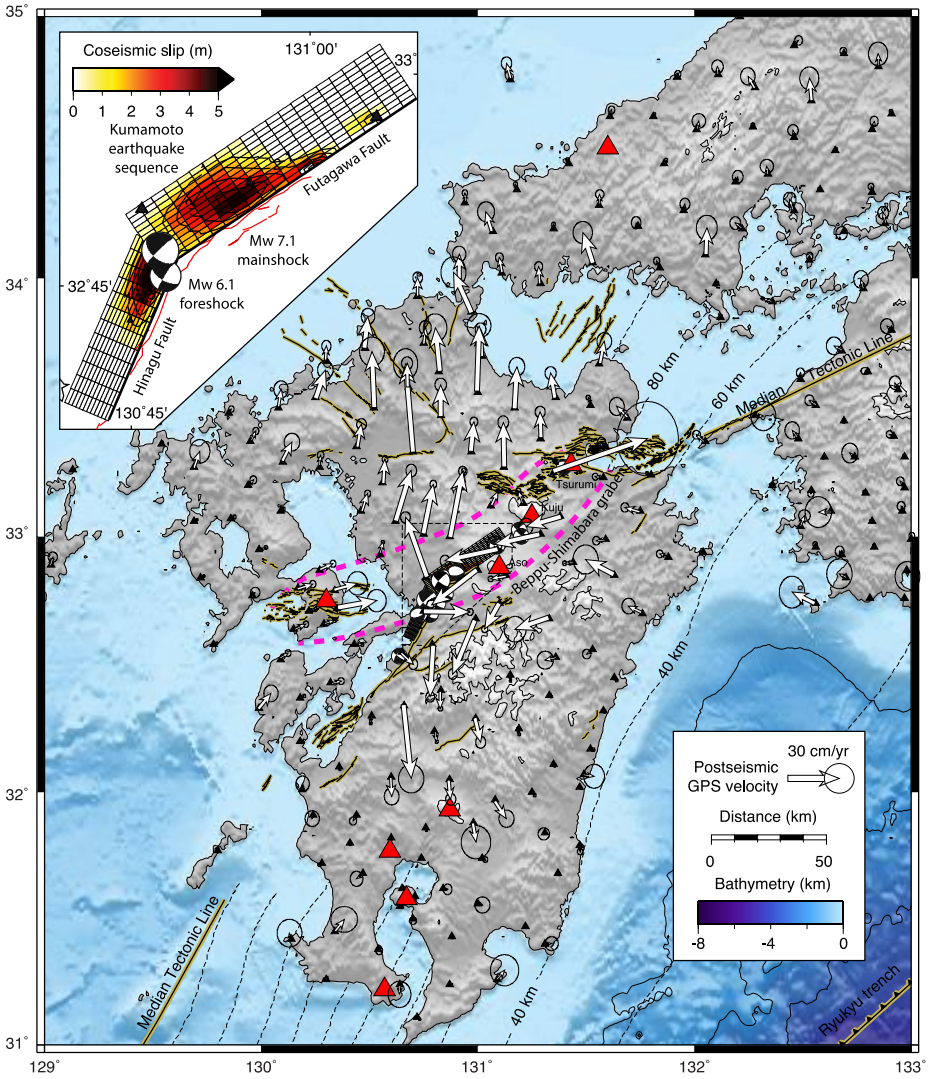


**Figure 1 – Postseismic deformation and coseismic slip from the 2016 Kumamoto earthquake sequence.**

Postseismic GPS velocities from the GEONET array (black triangles indicate stations, with white arrows for station velocities). The stations north of the rupture predominantly move rapidly northwards, while those south of the rupture move southwards with comparatively smaller velocities. Known faults are mapped in khaki, the subducting Ryukyu plate in dashed contours, and volcanoes are marked with red triangles. We have included the National Research Institute for Earth Science and Disaster Resilience (NIED) moment tensor solutions for the foreshock, mainshock, and large aftershocks with known tensor solutions. Smaller aftershocks with unknown mechanisms are marked with black stars. Pink dashed lines indicate the graben boundary. Inset illustrates the result of our geodetic inversion for the coseismic slip distribution on the Hinagu and Futagawa faults, including contributions from both the foreshock and mainshock.

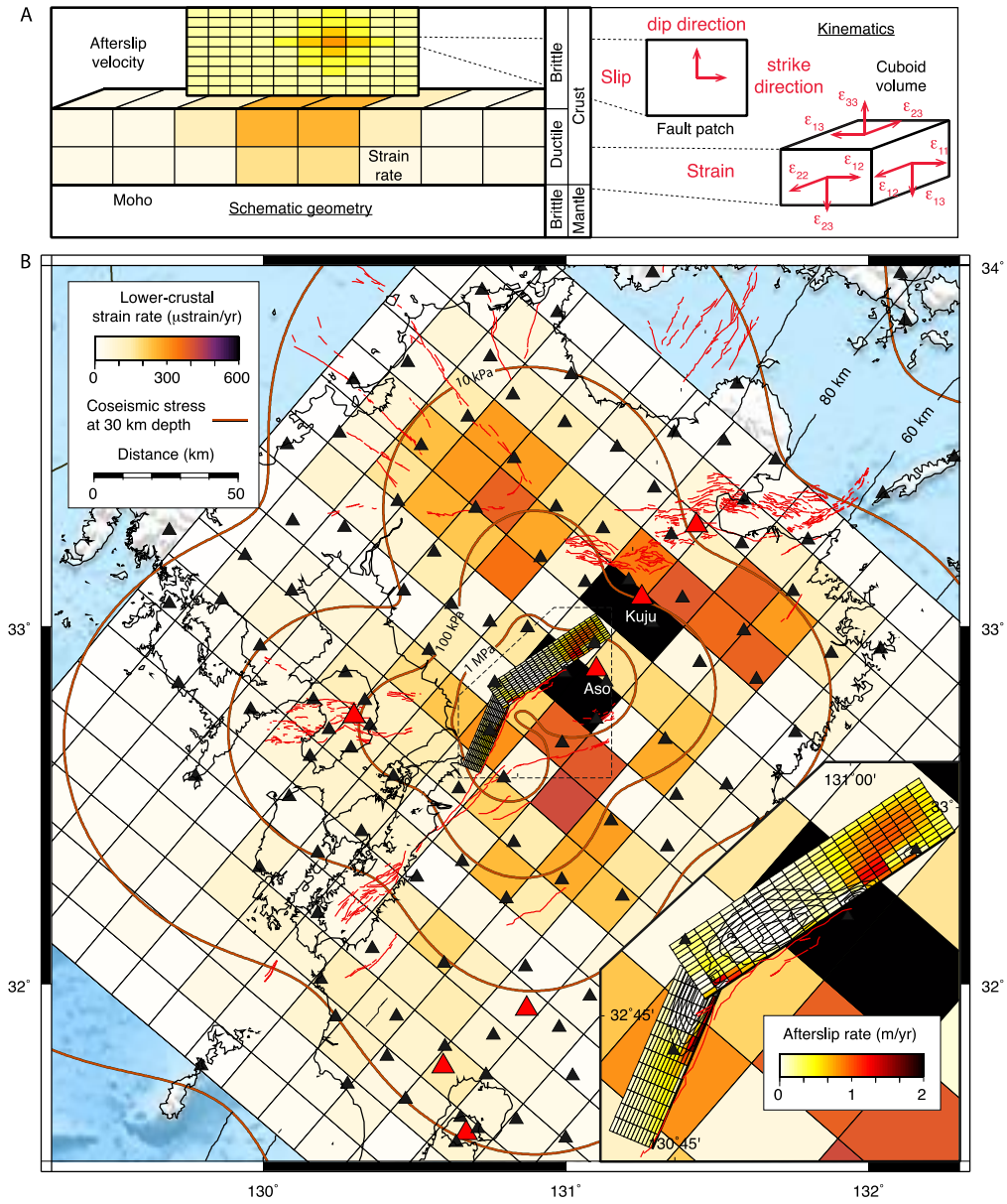


**Figure 2 – Distributed and localized deformation imaged as lower-crustal strain rates under Kyushu, with afterslip rates on the Hinagu and Futagawa faults, immediately following the 2016 Kumamoto earthquake sequence.**

(A) Schematic geometry of the lower crustal strain volumes and upper crustal faults. Right-hand side illustrates the six degrees of freedom for a deformable strain zone, and two degrees of freedom for a fixed fault patch. (B) Strain rates in the lower crustal strain volumes (depth 20-40km) are shown using the second invariant of the strain tensor in map view with afterslip rates on the fault and contours of coseismic slip (lower-right inset). Distribution of strain rates track the orange contours of coseismic stress change (assumed rigidity of 30GPa) closely, with two notable exceptions: higher strain rates are observed beneath Mt Aso and Mt Kuju. GPS stations are indicated with black triangles, known faults mapped with red lines, and volcanoes with red triangles.

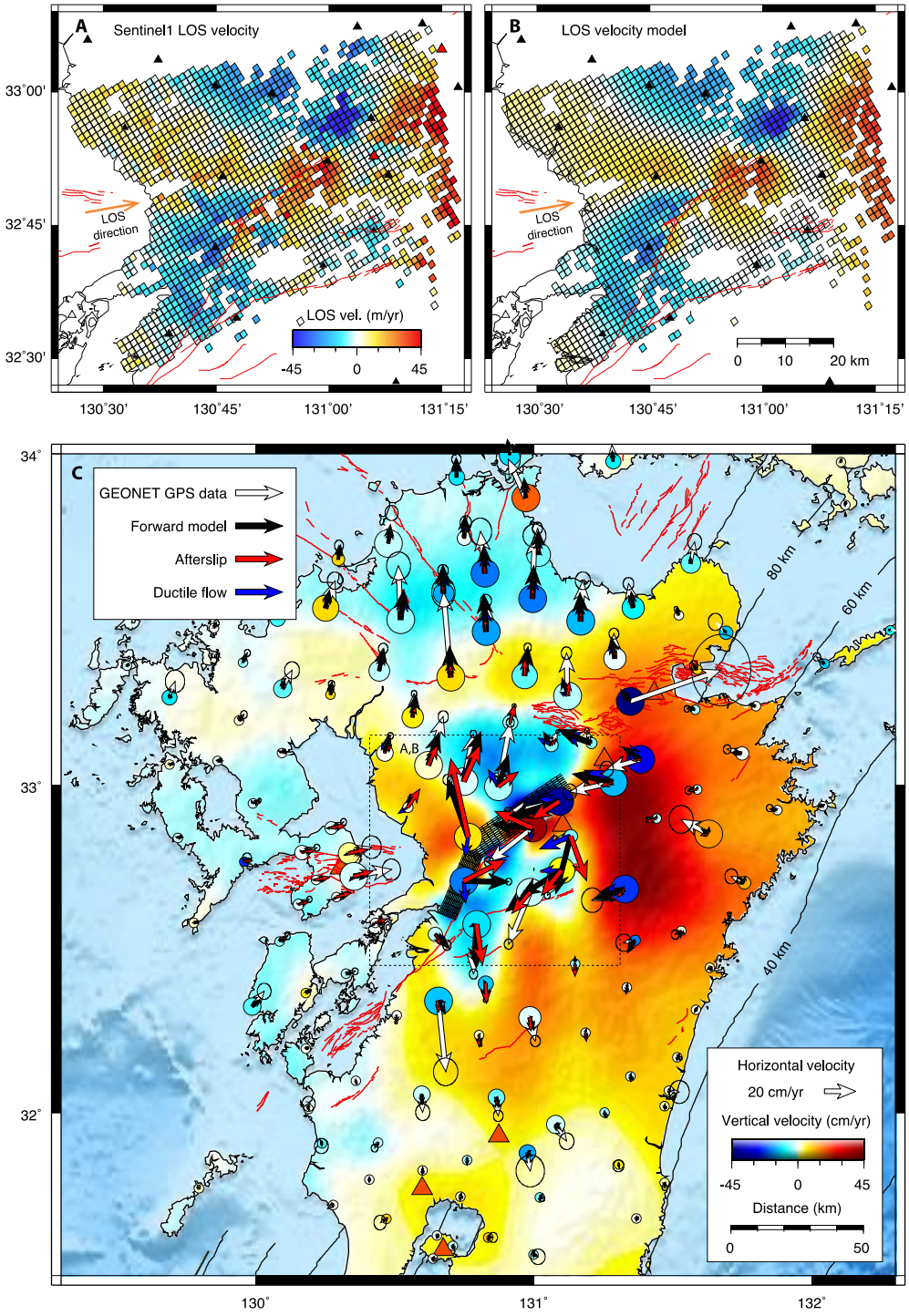


**Figure 3 – Observed and modelled postseismic velocities.**
(A) Unwrapped Sentinel-1A line-of-sight (LOS) InSAR velocity composite from three acquisitions between 20th April 2016 and 7th June 2016. GPS stations are indicated with black triangles, known faults mapped with red lines, LOS vectors with orange arrows, and volcanoes with red triangles. (B) LOS postseismic velocity model, with contributions from afterslip and ductile flow in lower crustal strain volumes. The model captures the key features of the observations, excepting some high-frequency fluctuations, especially those following the fault traces of the Hinagu and Futagawa faults. (C) Postseismic observed and modelled GPS velocities. Observational data are shown with white arrows and recovered

velocities in black. Contributions due to afterslip on the Hinagu and Futagawa faults and ductile flow in the lower crustal strain volumes are shown in red and blue respectively. Sub-areal background colour scale represents modelled uplift/subsidence velocity across Kyushu, where coloured circles represent observed vertical velocity at GPS stations.

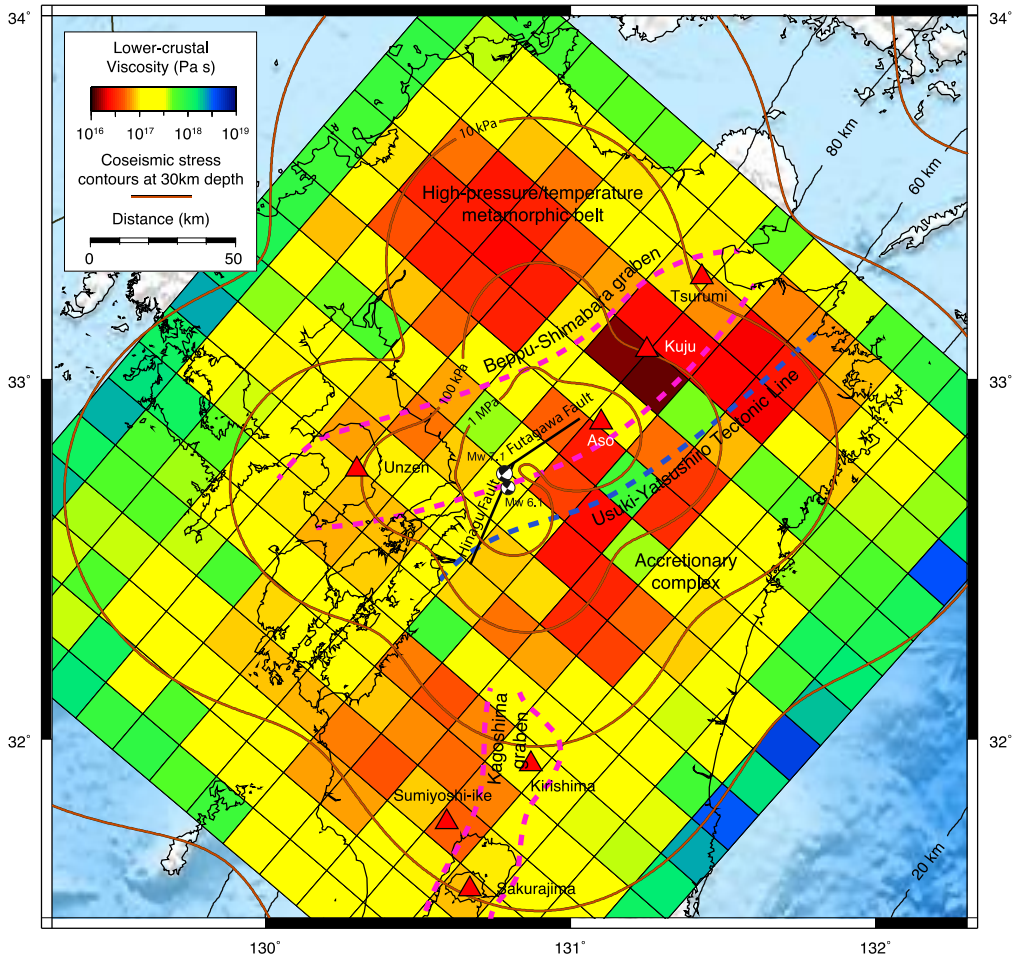


**Figure 4 – Transient viscosity structure of the lower crust**

Transient viscosity of the lower crust with volcanoes marked in red triangles, the Hinagu and Futagawa faults in black, and coseismic stress contours in orange. The regions of low viscosity follow the pattern of coseismic stress change modulated by the distribution of arc volcanism and plutonic bodies in Kyushu, with noticeable low viscosity anomalies beneath Mt Aso and Mt Kuju.

Supplementary Materials for

# Imaging the Distribution of Transient Viscosity Following the 2016 Mw 7.1 Kumamoto Earthquake

James D. P. Moore[1*], Hang Yu[2], Chi-Hsien Tang[3], Teng Wang[1], Sylvain Barbot[1*], Dongju Peng[1], Sagar Masuti[1], Justin Dauwels[2], Ya-Ju Hsu[3], Valère Lambert[1], Priyamvada Nanjundiah[1], Shengji Wei[1], Eric Lindsey[1], Lujia Feng[1] and Bunichiro Shibazaki[4].

* correspondence to: earth@jamesdpmoore.com and sbarbot@ntu.edu.sg

**This PDF file includes:**

Materials and Methods
Supplementary Text
Figs. S1 to S12

**Other Supplementary Materials for this manuscript includes the following:**

No additional Supplementary Materials

# Materials and Methods

## 1 Coseismic Data Processing

### 1.1 GPS Processing

For the coseismic analysis, we focus on a subset of stations close to the rupture. We processed GPS data between 10th April 2016 and 20th April 2016 from the 49 Japanese GEONET stations with detectable offsets on the 14th April 2016 using the GPS-Inferred Positioning System and Orbit Analysis Simulation Software (GIPSY-OASIS) version 6.2 [34]. We followed the GPS processing strategy described in [35]. By differencing the pre-foreshock and post-mainshock daily solutions, we estimated coseismic offsets that combine the effects from the mainshock and two foreshocks (Mw 6.2 and 6.0 on 14th April 2016).

### 1.2 InSAR Processing

We processed Interferometric Synthetic Aperture Radar (InSAR) data from the Japanese Aerospace Agency (JAXA) Advanced Land Observing Satellite 2 (ALOS-2) using GMTSAR software [36]. We used data from descending path 23 (frames 2950-2960, acquired 7th March 2016 and 18th April 2016) and path 29 (frames 2910-2920, acquired 14th January 2016 and 20th April, 2016), and ascending path 132 (frame 640, acquired 17th May 2015 and 17th April 2016). Data from path 29 was acquired in a left-looking direction, an unusual orientation highlighting the rapid acquisition capabilities of the ALOS-2 satellite. We formed interferograms from the Level 1.1 single-look-complex (SLC) images after first applying a five-parameter alignment to account for geometric and orbital errors in both range and azimuth, and ionospheric distortions which produce a second-order shift in azimuth. We applied a gaussian filter with a half-width of 300 m, and unwrapped the result using Statistical-Cost, Network-Flow Algorithm for Phase Unwrapping (SNAPHU) [37]. The resulting interferograms contained a residual ramp, which may be related to ionospheric distortions or orbital error; we removed a best-fitting plane from each image after masking out the deforming area. Finally, we down-sampled the line of sight displacement observations using a quadtree algorithm [38, 39] weighted by the median absolute deviation, a robust measure of the sample variance. The final number of resampled points contributing to the inversion were 399, 391, and 331 for paths 23, 29, and 132 respectively (Figure S1).

### 1.3 Coseismic Slip Inversion

We used two fault segments to follow the surface rupture, which is well observed by field investigation and shows a rotation of the strike of $\sim 30$ degrees near the epicenter of the mainshock. The southwest

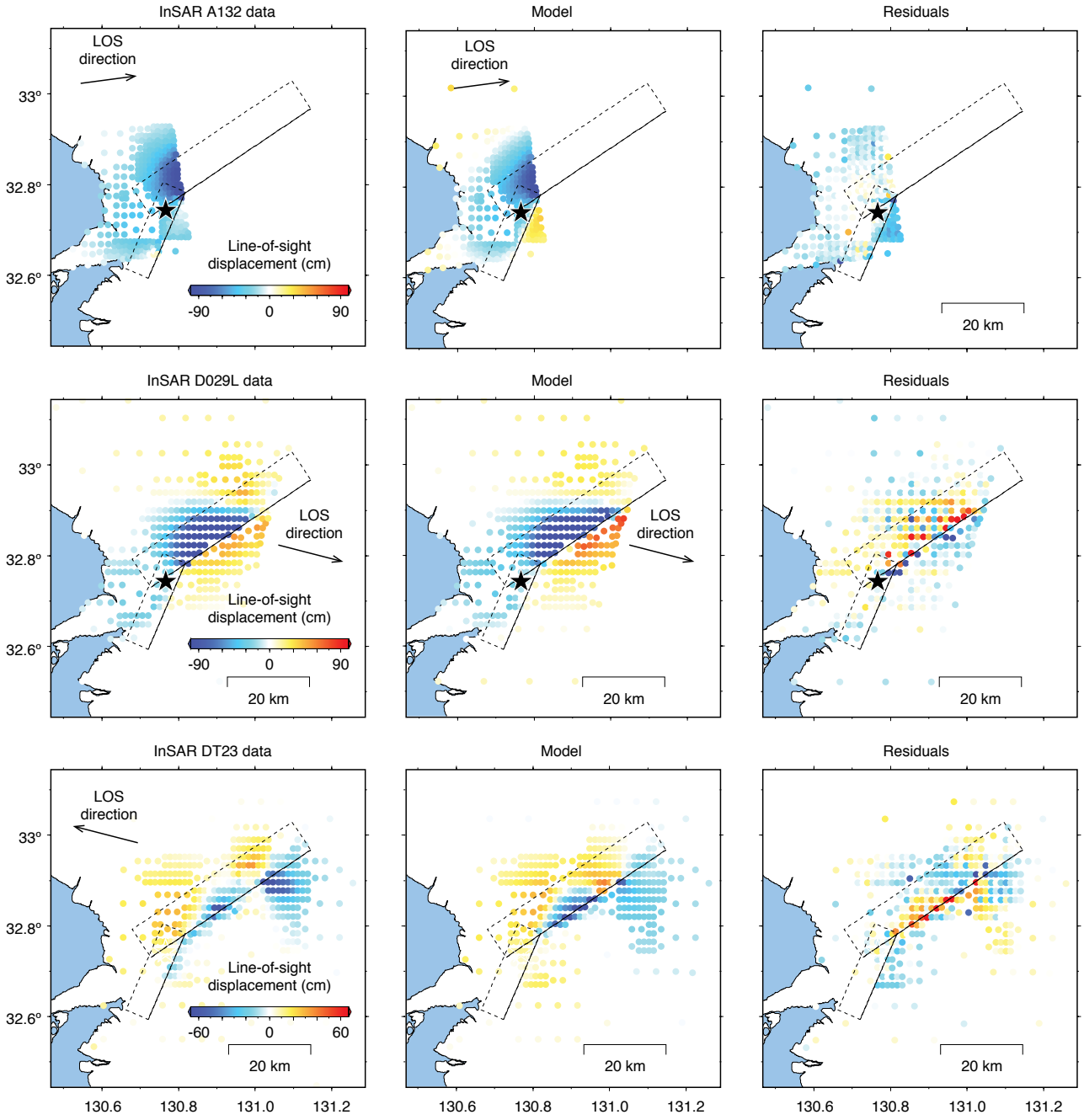


Figure S1: Processed InSAR and coseismic slip inversion. Columns from left to right are the data, model, and residuals.

segment has a strike of 203 degrees and dip of 75 degrees, and the northeast segment strikes 236 degrees and dips 69 degrees. The dip angles of these segments are obtained in a trial-and-error manner, guided by the depth distribution of the seismicity. We weighted each of data point equally, except that we weighted the GPS data five times larger than the InSAR data. The inversion was conducted with a simulated annealing inversion algorithm [40] in which we allow the rake and slip to vary within certain ranges. We tested different smoothing parameters and we choose a value that balances the misfit and roughness of the slip model (Fig. S2). The coseismic slip model shows a major asperity near the epicenter on the northeast segment, with most of the slip shallower than

10 km. The moment on the southwest segment is about 50% of that on the northeast segment with slightly deeper slip distribution. The coseismic slip distribution model can be found in ASCII form in the online repository *https://github.com/geodynamics/relax*.

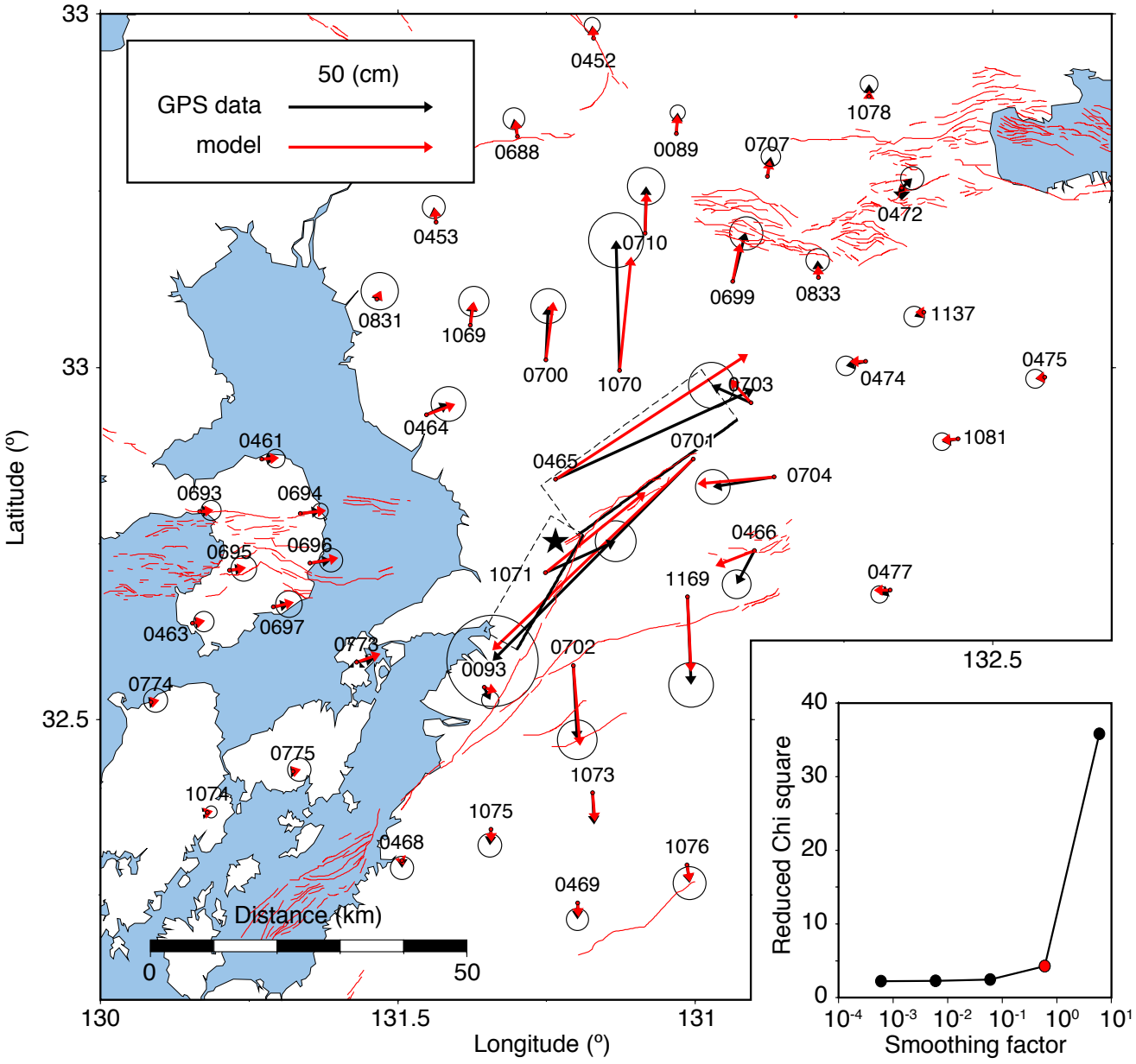


Figure S2: Coseismic GPS observed (black) and modeled (red) offsets. The final coseismic slip distribution model is chosen by exploration of the tradeoff between quality of fit and model smoothness (L curve). The final model is the one highlighted in red.

# 2 Postseismic Data Processing

## 2.1 InSAR Processing

We processed InSAR images from the European Sentinel-1A satellite ascending track T156, bursts 2 to 4. All the images were acquired using Terrain Observation by Progressive Scan (TOPS) technique,

which illuminates the ground in consecutive bursts of 20 km long with 1.5 km overlaps in the azimuth direction. The first image acquired only 4 days after the earthquake largely preserved much of the post-seismic motion. Three bursts covering the epicenter area were extracted and processed independently with the first image used as the master. We coregistered the interferometric pairs using a geometric approach with precise orbit ephemerides and an SRTM DEM of 3 arc second posting [41]. We multilooked all interferograms to a ground pixel size of 90 m × 90 m. We selected pixels with coherence larger than 0.3 and unwrapped the phases on these pixels using SNAPHU [37]. We manually corrected any visible unwrapping errors by adding or subtracting a full phase cycle before converting to line-of-sight deformation. Before modelling we downsampled the derived deformation map using a uniformly distributed 200m × 200m grid and corrected for the linear phase trend due to orbital errors on the three bursts based on GPS data points within the frames.

## 2.2 GPS Processing

We processed raw data from 321 continuous GPS stations operated by the Geospatial Information Authority (GSI) of Japan for the period from January 2013 to July 2016. The GPS Inferred Positioning System and Orbit Analysis Simulation Software(GIPSY-OASIS) version 6.2 developed by the Jet Propulsion Laboratory (JPL) was used for the static precise point positioning mode and the JPL final precise satellite orbits and clocks were held fixed in the data processing [34].

The employed observables were un-differenced ionosphere-free carrier phase (LC) and un-differenced ionosphere-free pseudo-range (PC). The phase center variations of both satellite and receiver antennas were corrected with the International GNSS Service reference frame 2008 (IGS08) absolute phase centre models [42]. Tidal effects from solid Earth, pole and ocean tides were removed. Solid Earth and pole tides were modelled according to International Earth Rotation and Reference System Service (IERS) 2010 conventions, ocean tide loading was calculated by the Onsala Space Observatory (`http://holt.oso.chalmers.se/loading/`) using the FES2004 model with respect to the center of mass of the solid Earth, atmosphere, and ocean combined. Tropospheric wet zenith delays and horizontal gradients were estimated as random-walk parameters with applying a prior zenith hydrostatic delays. Tropospheric zenith delays were mapped to slant delays down to a minimum elevation angle of 7° using the updated Vienna mapping functions in a grid file database [43]. Single-receiver ambiguity resolution was applied to resolve phase ambiguities.

The resulting fiducial-free daily positions were transformed to the International Terrestrial Reference Frame 2008 [44] using daily transformation parameters provided by JPL.

## 2.3 GPS Post-Processing

We use the weighted least squares method to analyse positioning time series at each GPS station with

$$\begin{aligned} X(t) =& X_0 + V_0\, t + \sum_{n=1}^{2} \left[ S_n \sin\left(n\omega t\right) + C_n \cos\left(n\omega t\right) \right] + \sum_{i=1}^{N_{\text{off}}} O_i H\left(t - t_i^{\text{off}}\right) \\ &+ \sum_{j=1}^{N_{\text{eq}}} \left[ E_j H\left(t - t_j^{\text{eq}}\right) + A_j H\left(t - t_j^{\text{eq}}\right) \left(1 - \exp\left(-\frac{t - t_j^{\text{eq}}}{t_c}\right)\right)\right], \end{aligned} \tag{1}$$

where $X_0$ is an intercept and $V_0$ denotes an interseismic velocity. $S_n$ and $C_n$ denote the scales of annual and semi-annual periodic motions, while $\omega = 2\pi/T$ with $T$ of one year. $N_{\text{off}}$ and $N_{\text{eq}} = 1$ are the offsets due to instrument or nontectonic changes and earthquakes, respectively ($N_{\text{off}}$ varies for each station). $O_i$ and $E_j$ are the amplitudes of the Heaviside step function $H(t)$ at time $t_i^{\text{off}}$ and $t_j^{\text{eq}}$, and $A_j$ are the coefficients of the postseismic transients described by an exponential decay at time $t_j^{\text{eq}}$. We use the grid search method to find an optimised curve for postseismic transient with its characteristic time $t_c$ to fit the data. After decomposing the interseismic secular motion, coseismic displacements of foreshock and mainshock, and periodic motion in the GPS data, we derive the 91-day postseismic displacement after the Kumamoto earthquake. Also, by a first derivative function of exponential decay,

$$v(t) = \frac{A}{t_c} \exp\left(-\frac{t - t^{eq}}{t_c}\right), \tag{2}$$

we derive an initial postseismic velocity

$$v(t^{eq}) = \frac{A}{t_c}, \tag{3}$$

where $A$ is the amplitude of the postseismic transient at each station. This velocity field does not require a reference point as any plate motions will be absorbed by $V_0$. The uncertainties of each component were estimated by error propagation,

$$\mathbf{C_m} = \left(\mathbf{G}^T \mathbf{C}_d^{-1} \mathbf{G}\right)^{-1}, \tag{4}$$

where $\mathbf{G}$ represents the design matrix for time series regression, $\mathbf{C}_m$ and $\mathbf{C}_d$ are the covariance matrixes for model and data, respectively. An example for the GPS post-processing at station 0701 may be found in Figure S3.

## 2.4 InSAR Post-Processing

We consider four Sentinel-1A SAR images acquired in 2016 in April 20th, May 2nd, May 14th, and June 7th. We build a time series of line-of-sight displacement using the interferometric pairs always formed with the first acquisition following the mainshock. Due to the rapid repeat pass of Sentinel-1A, we obtain interferograms for 12, 24, and 48 days following April 20th, 2016. To obtain a line-of-sight velocity field, we estimate the amplitude of an exponential cumulative postseismic displacement with a characteristic time decay of two years. The velocity field is obtained by taking the derivative analytically, same as for the GPS post-processing. Because the InSAR time series misses a few days of postseismic relaxation, we expect some discrepancies with the GPS velocity field. This problem is mitigated by tying the InSAR velocity field to the GPS velocity field at $t = t_{\text{eq}}$ for the long wavelengths using a bilinear ramp. As the InSAR only constrains the near-field deformation, we expect the remaining discrepancy at short wavelength to affect mostly afterslip, with minimal impact on our estimate of the effective viscosity in the lower crust throughout Kyushu.

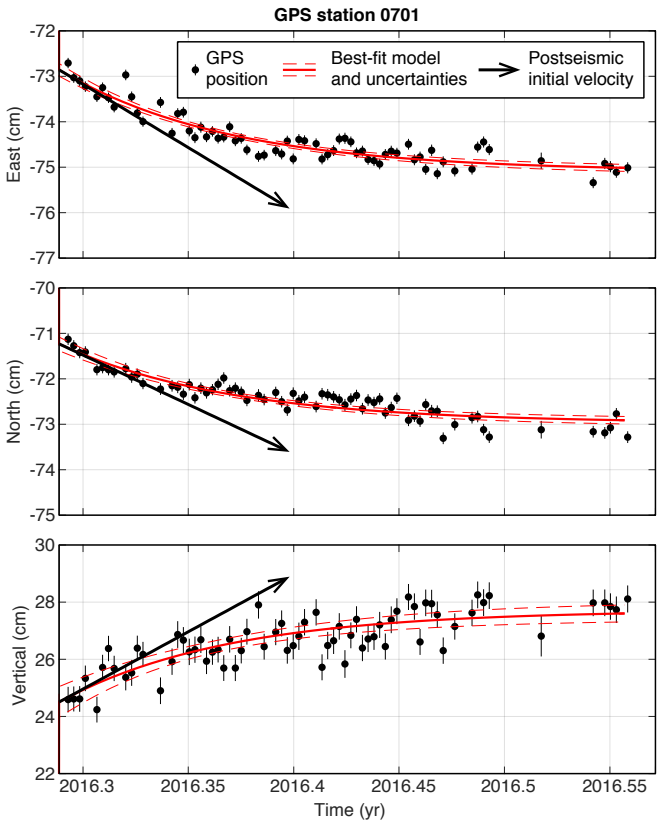


Figure S3: Fit to GPS data using exponential kernels, after removal of seasonal signal, secular motion and offsets due to instrument maintenance. Observational data points are marked in black with best fit kernels in red lines, 95% confidence in dashed lines, and instantaneous post-seismic velocity with black vectors. GPS station 0701 is located near the Futagawa fault (Fig. S2).

# 3 Static Inversion of Fault Slip and Distributed Strain

We build on well-established geodetic inversion techniques [31, 32, 33] to incorporate strain in finite volumes. We consider the model space

$$\mathbf{m} = \begin{pmatrix} \mathbf{m}_s \\ \mathbf{m}_d \\ \mathbf{m}_{11} \\ \mathbf{m}_{12} \\ \mathbf{m}_{13} \\ \mathbf{m}_{22} \\ \mathbf{m}_{23} \\ \mathbf{m}_{33} \end{pmatrix} \tag{5}$$

where $\mathbf{m}_s$ and $\mathbf{m}_d$ are the strike- and dip-directions of afterslip, and $\mathbf{m}_{ij}$, $ij \in \{11, 12, 13, 22, 23, 33\}$, are the $ij$ components of strain in all finite volumes. We call $\mathbf{m}_f$, the vector containing strike slip and dip slip, and $\mathbf{m}_s$, the vector containing the strain components. The surface deformation data are a linear combination of the model parameters

$$\mathbf{d} = \mathbf{G}\,\mathbf{m} = \mathbf{G} \begin{pmatrix} \mathbf{m}_f \\ \mathbf{m}_s \end{pmatrix} \tag{6}$$

where the design matrix is given by

$$\mathbf{G} = \begin{pmatrix} \mathbf{G}_\mathrm{s} & \mathbf{G}_\mathrm{d} & \mathbf{G}_{11} & \mathbf{G}_{12} & \mathbf{G}_{13} & \mathbf{G}_{22} & \mathbf{G}_{23} & \mathbf{G}_{33} \end{pmatrix} \tag{7}$$

and the $\mathbf{G}_X$, $X \in \{s, d, 11, 12, 13, 22, 23, 33\}$ are the kernels connecting strike slip and dip slip on faults, and strain in the 11, 12, 13, 22, 23, and 33 directions to surface displacements. We use the formulation of Okada [24] to build the matrices $\mathbf{G}_\mathrm{s}$ and $\mathbf{G}_\mathrm{d}$. The others are obtained analytically using our own formulation for cuboid strain volumes [25]. The data consist of GPS and InSAR observations and the above kernels are declined accordingly.

Displacement kernels for cuboid strain volumes may be found in Figure S4, where each panel corresponds to one independent component of strain. The displacement fields for each component of strain bears a resemblance to many existing elastic solutions, with the $\epsilon_{12}$ component resembling strike-slip faulting, $\epsilon_{13}$ and $\epsilon_{23}$ dip-slip faulting, $\epsilon_{11}$ and $\epsilon_{22}$ diking, and $\epsilon_{33}$ a Mogi source. This is expected, as these strain volumes are entirely general and encompass the full range of inelastic deformation within their interior.

To avoid overfitting the data, we consider the following constraints for fault slip. First, we minimise the afterslip stress change with

$$\frac{1}{\alpha_1}\mathbf{Q}_s\mathbf{m}_f = \frac{1}{\alpha_1}\begin{pmatrix} \mathbf{K}_{ss} & \mathbf{K}_{sd} \\ \mathbf{K}_{ss} & \mathbf{K}_{sd} \end{pmatrix}\mathbf{m}_f = \mathbf{0}\ , \tag{8}$$

where $\mathbf{K}_{ab}$, $a, b \in \{s, d\}$ is the kernel describing the change of traction in the $a$ direction due to

afterslip in the $b$ direction, with $s$ and $d$ the strike and dip directions, respectively. Hyperparameter $\alpha_1$ controls the weight of this constraint, which favours a smooth distribution of afterslip. We use the formulation of Okada [24] to construct the matrices $\mathbf{K}_{ab}$. We penalise slip in the regions of high coseismic slip

$$\frac{1}{\gamma}\mathbf{Q}_p\mathbf{m}_f = \frac{1}{\gamma}\begin{pmatrix}\mathbf{C}_p & \mathbf{0}\\ \mathbf{0} & \mathbf{C}_p\end{pmatrix}\mathbf{m}_f = \mathbf{0}\ , \tag{9}$$

where $\mathbf{C}_p$ contains zeros in areas of positive Coulomb stress change and values proportional to Coulomb stress in areas of negative Coulomb stress change. This allows smooth overlap between regions of coseismic slip and afterslip. Hyperparameter $\gamma$ controls the weight of this constraint. We penalise afterslip directions that are orthogonal to the coseismic stress change using

$$\frac{1}{\gamma_2}\mathbf{Q}_a\mathbf{m}_f = \frac{1}{\gamma_2}\begin{pmatrix}\mathbf{D}_s & \mathbf{D}_d\end{pmatrix}\mathbf{m}_f = \mathbf{0}\ , \tag{10}$$

where $\mathbf{D}_s$ and $\mathbf{D}_d$ are to project slip in the direction orthogonal to the coseismic shear stress on the fault. Hyperparameter $\gamma_2$ controls the weight of this constraint.

For strain in finite volumes, we minimise the postseismic stress change with the additional constraint

$$\frac{1}{\alpha_2}\mathbf{R}_s\mathbf{m}_s = \frac{1}{\alpha_2}\begin{pmatrix}\mathbf{K}_{1111} & \mathbf{K}_{1112} & \mathbf{K}_{1113} & \mathbf{K}_{1122} & \mathbf{K}_{1123} & \mathbf{K}_{1133}\\ \mathbf{K}_{1211} & \mathbf{K}_{1212} & \mathbf{K}_{1213} & \mathbf{K}_{1222} & \mathbf{K}_{1223} & \mathbf{K}_{1233}\\ \mathbf{K}_{1311} & \mathbf{K}_{1312} & \mathbf{K}_{1313} & \mathbf{K}_{1322} & \mathbf{K}_{1323} & \mathbf{K}_{1333}\\ \mathbf{K}_{2211} & \mathbf{K}_{2212} & \mathbf{K}_{2213} & \mathbf{K}_{2222} & \mathbf{K}_{2223} & \mathbf{K}_{2233}\\ \mathbf{K}_{2311} & \mathbf{K}_{2312} & \mathbf{K}_{2313} & \mathbf{K}_{2322} & \mathbf{K}_{2323} & \mathbf{K}_{2333}\\ \mathbf{K}_{3311} & \mathbf{K}_{3312} & \mathbf{K}_{3313} & \mathbf{K}_{3322} & \mathbf{K}_{3323} & \mathbf{K}_{3333}\end{pmatrix}\mathbf{m}_s = \mathbf{0}\ , \tag{11}$$

where the $\mathbf{K}_{ab}$, $a, b \in \{11, 12, 13, 22, 23, 33\}$ are the kernels relating stress in the direction $a$ at the centre of every finite volume due to strain in the direction $b$ in each finite volume, which we compute analytically [24]. The hyperparameter $\alpha_2$ controls the strength of this constraint, which favours smooth distributions of strain. We penalise the side edges of the mesh representing the lower crust with the constraint $\frac{1}{\alpha_4}\mathbf{R}_p\mathbf{m}_s = \mathbf{0}$, with associated hyperparameter $\alpha_4$. We penalise isotropic strain using the constraint

$$\frac{1}{\beta}\mathbf{R}_d\mathbf{m}_s = \frac{1}{\beta}\begin{pmatrix}\mathbf{I} & \mathbf{0} & \mathbf{0} & \mathbf{I} & \mathbf{0} & \mathbf{I}\end{pmatrix}\mathbf{m}_s = \mathbf{0}\ , \tag{12}$$

where $\mathbf{I}$ is the identity matrix and $\beta$ the hyperparameter controlling the weight of this constraint. Finally, we penalise strain directions that are orthogonal to the coseismic deviatoric stress change

$$\frac{1}{\lambda}\mathbf{R}_a\mathbf{m}_s = \frac{1}{\lambda}\begin{pmatrix}\mathbf{P}^1_{11} & \mathbf{P}^1_{12} & \mathbf{P}^1_{13} & \mathbf{P}^1_{22} & \mathbf{P}^1_{23} & \mathbf{P}^1_{33}\\ \mathbf{P}^2_{11} & \mathbf{P}^2_{12} & \mathbf{P}^2_{13} & \mathbf{P}^2_{22} & \mathbf{P}^2_{23} & \mathbf{P}^2_{33}\\ \mathbf{P}^3_{11} & \mathbf{P}^3_{12} & \mathbf{P}^3_{13} & \mathbf{P}^3_{22} & \mathbf{P}^3_{23} & \mathbf{P}^3_{33}\\ \mathbf{P}^4_{11} & \mathbf{P}^4_{12} & \mathbf{P}^4_{13} & \mathbf{P}^4_{22} & \mathbf{P}^4_{23} & \mathbf{P}^4_{33}\\ \mathbf{P}^5_{11} & \mathbf{P}^5_{12} & \mathbf{P}^5_{13} & \mathbf{P}^5_{22} & \mathbf{P}^5_{23} & \mathbf{P}^5_{33}\end{pmatrix}\mathbf{m}_s = \mathbf{0}\ , \tag{13}$$

where the $\mathbf{P}^n_{ij}$, $n \in \{1, 2, 3, 4, 5\}$ are the components $ij$ of the 5 strain directions orthogonal to the coseismic deviatoric stress change and $\lambda$ is the hyperparameter controlling the overall weight of this

constraint, which also scales with the norm of the deviatoric coseismic stress tensor. We find these directions by singular value decomposition of the coseismic deviatoric stress tensor. Fig. S5 shows the orientations of the principal horizontal directions of the stress and strain-rate tensors, showing their relative alignment throughout the model.

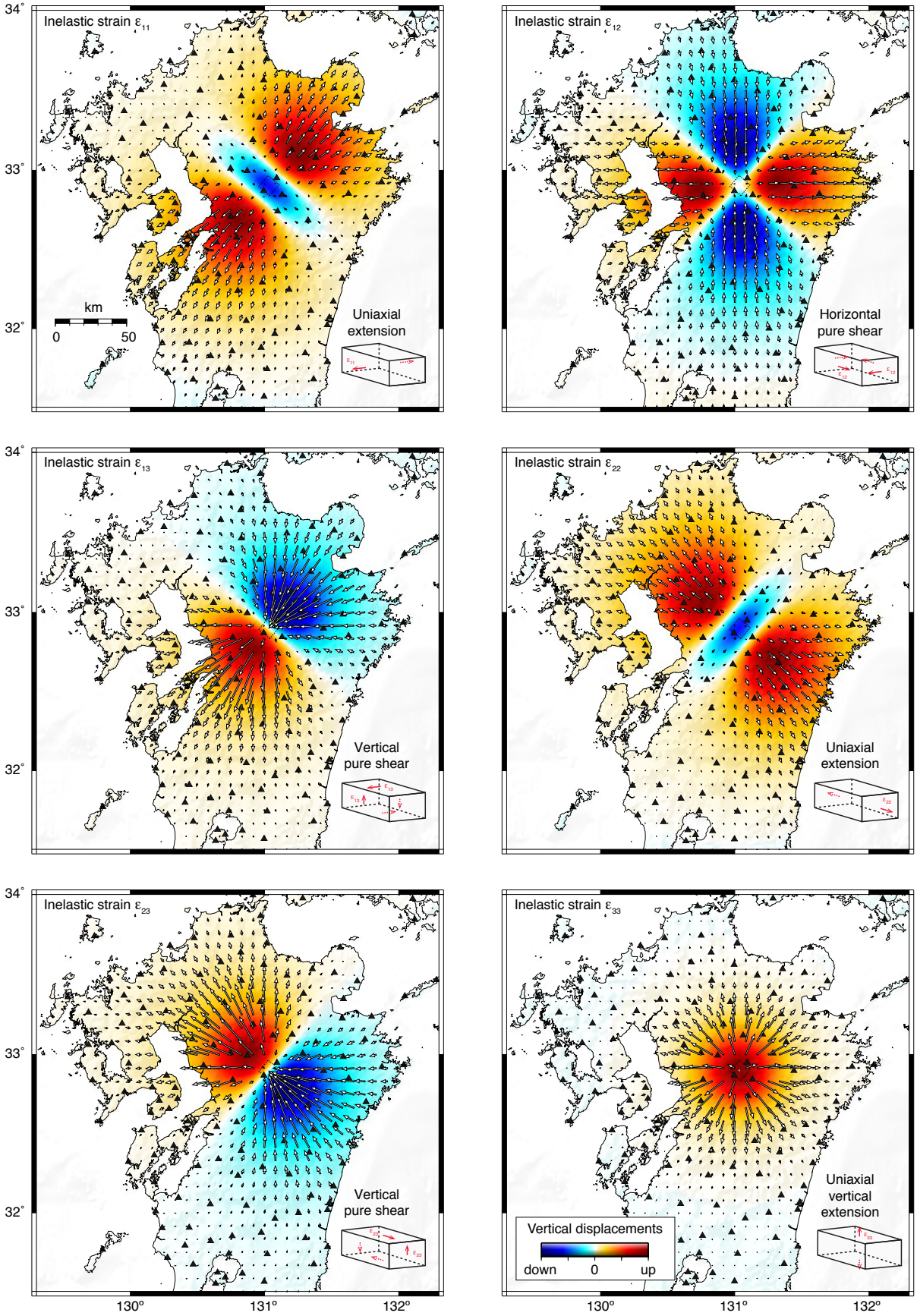


Figure S4: Displacement kernels for an example cuboid strain volume beneath Kyushu. Each panel corresponds to one independent component of strain. Horizontal displacements are given by white vectors and vertical displacements by the background colour map. Location of cuboid illustrated with dashed black line, at a depth of 30km.

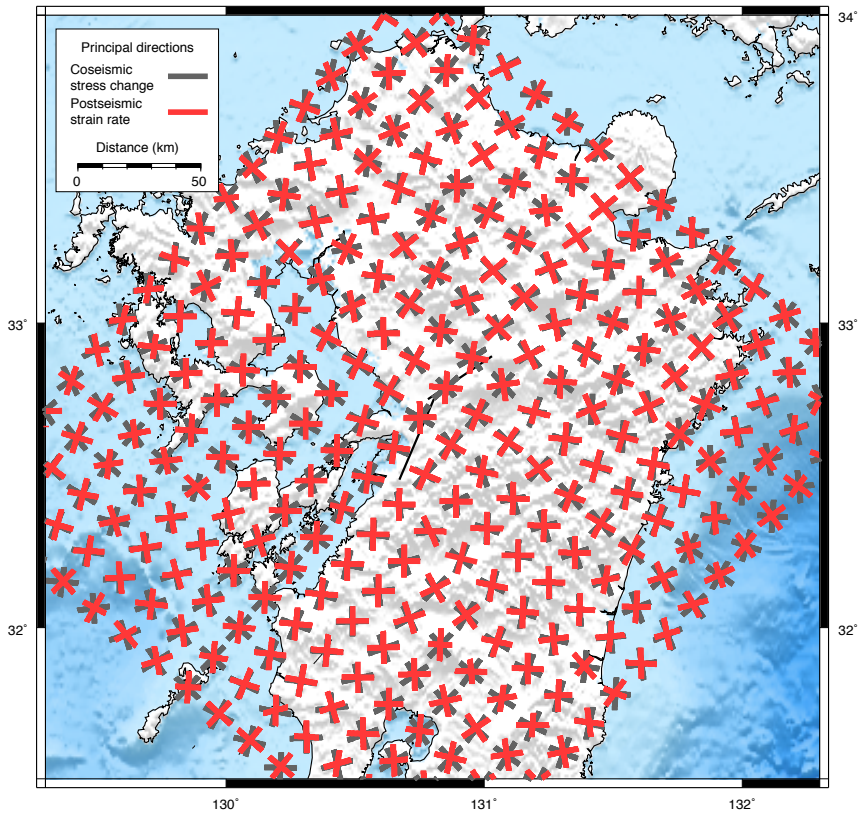


Figure S5: Principal directions of the stress (black) and strain-rate (red) tensors projected in map view. The strain rate is constrained to align with the stress change except in regions of low coseismic stress near the nodal planes and in the far field. The tensor directions differ in the near field, presumably due to fault complexity, the details of which are not fully captured in our coseismic slip model.

# 4 Outlier-Insensitive Bayesian Inversion of Geodetic Data

The observed data $\mathbf{d}$ are expressed as a linear combination of the model parameters $\mathbf{m}$ with two sources of additive noise:

$$\mathbf{d} = \mathbf{G}\mathbf{m} + \boldsymbol{\epsilon} + \boldsymbol{\delta}, \tag{14}$$

where $\boldsymbol{\epsilon}$ is a Gaussian white noise with mean zero and variance $v_\epsilon$, and $\boldsymbol{\delta}$ is the impulsive noise resulting from the outliers. Since we assume there exist few outliers, of arbitrary size, the vector $\boldsymbol{\delta}$ is supposed to be sparse. With this goal in mind, we assume that each entry $\delta_i$ in $\boldsymbol{\delta}$ follows a zero-mean Gaussian distribution with variance $v_{\delta i}$. We further impose non-informative Jeffrey's prior on the variance $v_{\delta i}$. After integrating out $v_{\delta i}$, we equivalently impose a Student's $t$-distribution on $\delta_i$ [45]. Such shrinkage priors promote sparsity, and the resulting $\boldsymbol{\delta}$ would become sparse.

For the model parameters $\mathbf{m}$, containing fault slip and strain in finite volumes, we can express their priors as Gaussian distributions that characterise the constraints defined in Section 3:

$$p(\mathbf{m}_f) \propto \det\left(\frac{1}{\alpha_1^2}\mathbf{K}_s + \frac{1}{\gamma^2}\mathbf{K}_p + \frac{1}{\gamma_2^2}\mathbf{K}_a\right)^{\frac{1}{2}} \exp\left[-\frac{1}{2}\mathbf{m}_f^T\left(\frac{1}{\alpha_1^2}\mathbf{K}_s + \frac{1}{\gamma^2}\mathbf{K}_p + \frac{1}{\gamma_2^2}\mathbf{K}_a\right)\mathbf{m}_f\right], \tag{15}$$

$$p(\mathbf{m}_s) \propto \det\left(\frac{1}{\alpha_2^2}\mathbf{J}_s + \frac{1}{\alpha_4^2}\mathbf{J}_p + \frac{1}{\beta^2}\mathbf{J}_d + \frac{1}{\lambda^2}\mathbf{J}_a\right)^{\frac{1}{2}} \exp\left[-\frac{1}{2}\mathbf{m}_s^T\left(\frac{1}{\alpha_2^2}\mathbf{J}_s + \frac{1}{\alpha_4^2}\mathbf{J}_p + \frac{1}{\beta^2}\mathbf{J}_d + \frac{1}{\lambda^2}\mathbf{J}_a\right)\mathbf{m}_s\right], \tag{16}$$

where the square matrices $\mathbf{K}_s = \mathbf{Q}_s^T\mathbf{Q}_s$, $\mathbf{K}_p = \mathbf{Q}_p^T\mathbf{Q}_p$, and $\mathbf{K}_a = \mathbf{Q}_a^T\mathbf{Q}_a$ characterise respectively the constraints of smoothness, coseismic area pinning, and penalisation of fault slip in the direction orthogonal to stress. The square matrices $\mathbf{J}_s = \mathbf{R}_s^T\mathbf{R}_s$, $\mathbf{J}_p = \mathbf{R}_p^T\mathbf{R}_p$, $\mathbf{J}_d = \mathbf{R}_d^T\mathbf{R}_d$, and $\mathbf{J}_a = \mathbf{R}_a^T\mathbf{R}_a$ characterise respectively the constraints of smoothness, edge pinning, deviatoric stress (penalisation of isotropic strain), and penalisation of strain directions orthogonal to coseismic stress on shear zone, and the hyperparameters described in Section 3, $\{\alpha_1,\ \gamma,\ \gamma_2,\ \alpha_2,\ \alpha_4,\ \beta,$ and $\lambda\}$ control the strength of these constraints. Non-informative Jeffrey's priors are also imposed on these hyperparameters.

Our objective is to infer the posterior distribution of all parameters conditioned on the observed data:

$$\begin{aligned} p(\mathbf{m}_f, \boldsymbol{m}_s, v_g, v_i, \mathbf{v}_\delta, \alpha_1, \gamma, \gamma_2, \alpha_2, \alpha_4, \beta, \lambda | \mathbf{d}) \propto \\ p(\mathbf{d}|\mathbf{m}_f, \mathbf{m}_s, v_g, v_i, \mathbf{v}_\delta)\, p(\mathbf{m}_f|\alpha_1, \gamma, \gamma_2)\, p(\mathbf{m}_s|\alpha_2, \alpha_4, \beta, \lambda) \\ p(\alpha_1)\, p(\gamma)\, p(\gamma_2)\, p(\alpha_2)\, p(\alpha_4)\, p(\beta)\, p(\lambda) \cdot p(v_\epsilon) \prod_k p(v_{\delta k})\ . \end{aligned} \tag{17}$$

We derive a Monte-Carlo Markov Chain algorithm [46] to draw samples from the posterior distribution (17). Specifically, we follow the Gibbs sampling approach by drawing a sample of each variable (or each block of variables) in turn, conditioned on the current values of other variables. For the model parameters $\mathbf{m}$, the resulting conditional distribution is a multivariate Gaussian distribution. For the hyperparameters and the noise variance, however, it is intractable to compute the analytical forms of the conditional distributions. We therefore employ a Metropolis-Hastings procedure and after obtaining a sufficient number of samples, in this case over $100,000$, we calculate the expectation of the desired quantities.

# 5 Synthetic Tests

## 5.1 Checkerboard Strain-Rate Test

The forward model for the checkerboard strain-rate tests were conducted by taking the coseismic stress change in the lower crustal strain volumes, normalising the stresses in each volume, and multiplying by a checkerboard function (1 or 0 in a grid). This produced four cuboid zones of distributed strain-rates shown in Figure S6, which were convolved with the displacement kernels (Figure S4) producing the simulated displacements, to which we added random noise and a selection of outliers. To avoid outlier selection bias we drew our outliers from a uniform distribution and randomly replaced 5% of the simulated displacements. This is a more extreme case than the observations where our algorithm identified 1.5% of the data as outliers. We then invert the synthetic displacement field using the algorithm described in Section 4. Once identified by the algorithm, outliers are entirely removed from the inversion and thus may be of arbitrary size. Since we assume there exist few outliers, if we have a large population of outliers in the data this will significantly increase the number of samples required to calculate the expectation of the desired hyperparameters, and if we had a substantial population of spatially correlated outliers this would correspondingly bias the solution. We evaluate a solution without outlier detection (Figure S6), and with outlier detection (Figure S7). We find that outliers can severely bias the solution strain field, and that our outlier-insensitive algorithm produces meaningful solutions. This gives us confidence that the results presented in the main section are robust.

## 5.2 Uniform Viscosity Test

The forward model for the uniform viscosity test was conducted by taking the coseismic stress change in the lower crustal strain volumes and scaling by a constant viscosity of $10^{17}$ Pa s. This produced a distinctive pattern of strain-rates, closely centred on the Hinagu and Futagawa faults, which were convolved with the displacement kernels (Figure S4) producing the simulated displacements. We analyse this displacement field through our inversion algorithm using the outlier detection algorithm described in Section 4. The result of this test is shown in Figure S8. This test field is recovered more clearly than the checkerboard as our prior assumes a smooth distribution of strain rates. The recovered transient viscosity distribution, assuming a steady-state uniform viscosity of $10^{19}$ Pa s, is illustrated in Figure S9. The inversion recovers the uniform viscosity of $1 \times 10^{17}$ Pa s in a large region centered on the epicenter.

## 5.3 Spatially Varying Viscosity Test

The forward model for the spatially varying viscosity test was conducted by taking the coseismic stress change in the lower crustal strain volumes and scaling by a spatial distribution of viscosity parallel to the volcanic arc. For the forward model we used a background transient viscosity of $10^{18}$ Pa s and an arc-parallel transient viscosity of $10^{16} - 10^{17}$ Pa s. We convolved the strain-rates with the displacement kernels (Figure S4) to produce the simulated displacements. We analyse this displacement field through our inversion algorithm using the outlier detection algorithm described

in Section 4. The recovered transient viscosity distributions, assuming a background steady-state uniform viscosity of $10^{19}$ Pa s, is illustrated in Figure S10. These tests show that we are able to resolve viscosity variations to within half an order of magnitude, or 30%, of the true value. The exception to this being at the very edges of the inversion, which are dominated by our assumption for the background steady-state viscosity due the the low coseismic stress change in this region. The assumption of smooth variation of strain-rates correspondingly smooths the recovered viscosities when there are large step changes in the model, thus for this model geometry we do not expect to be able to resolve short wavelength variations in viscosity smaller than 30 km, a wavelength commensurate with the average spacing of the GEONET stations and with the depth of the lower crust.

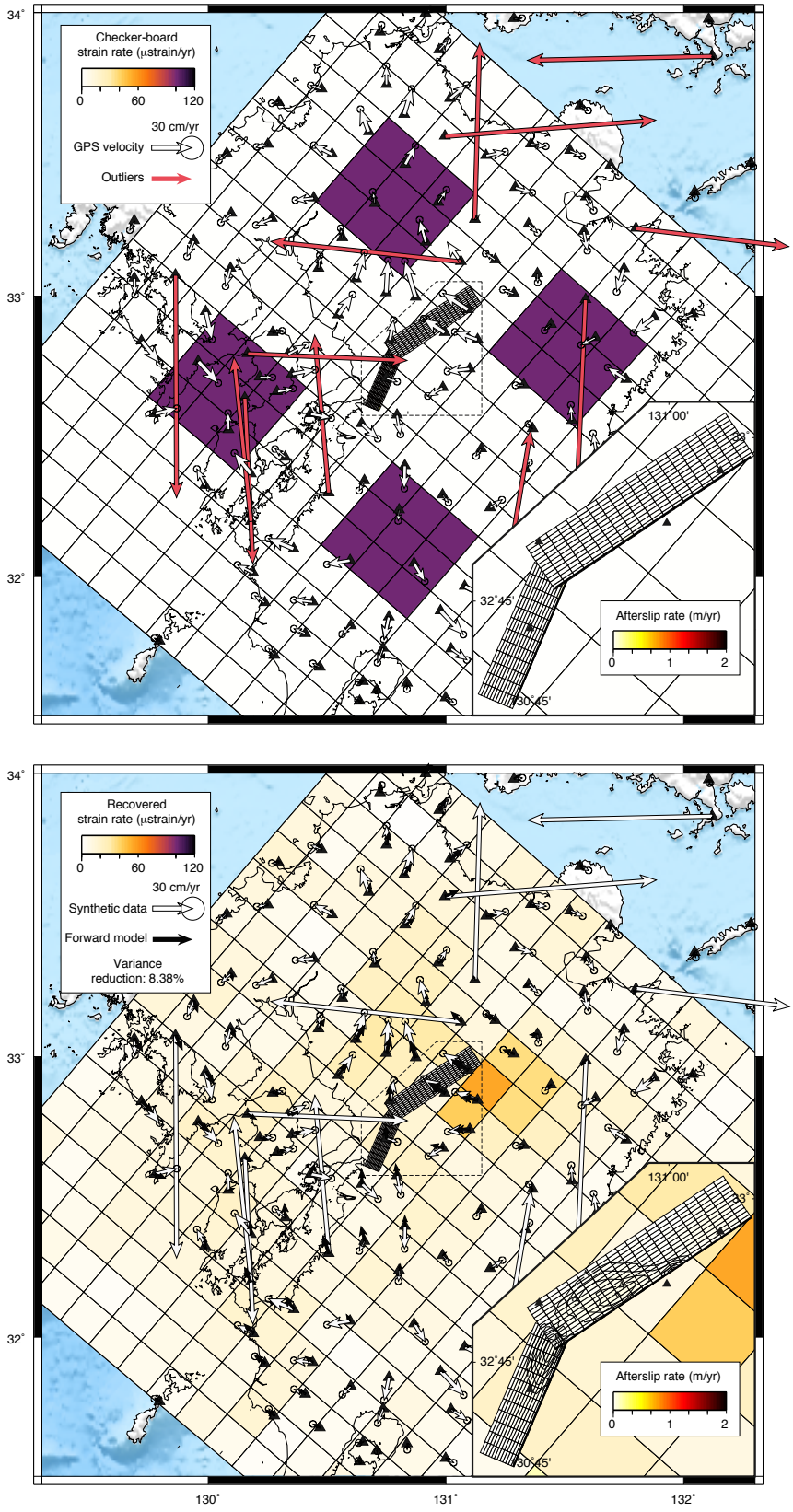


Figure S6: Checkerboard strain-rate test with outliers, but no outlier detection. Strain rates in the lower crustal strain volumes (20-40km) are shown in map view with afterslip rates on the fault and contours of coseismic slip (lower-right inset). GPS stations are indicated with black triangles. Upper pane shows strain-rate model set-up and calculated displacements with white arrows, outliers are included as red arrows. Lower pane shows recovered model and displacements in black arrows.

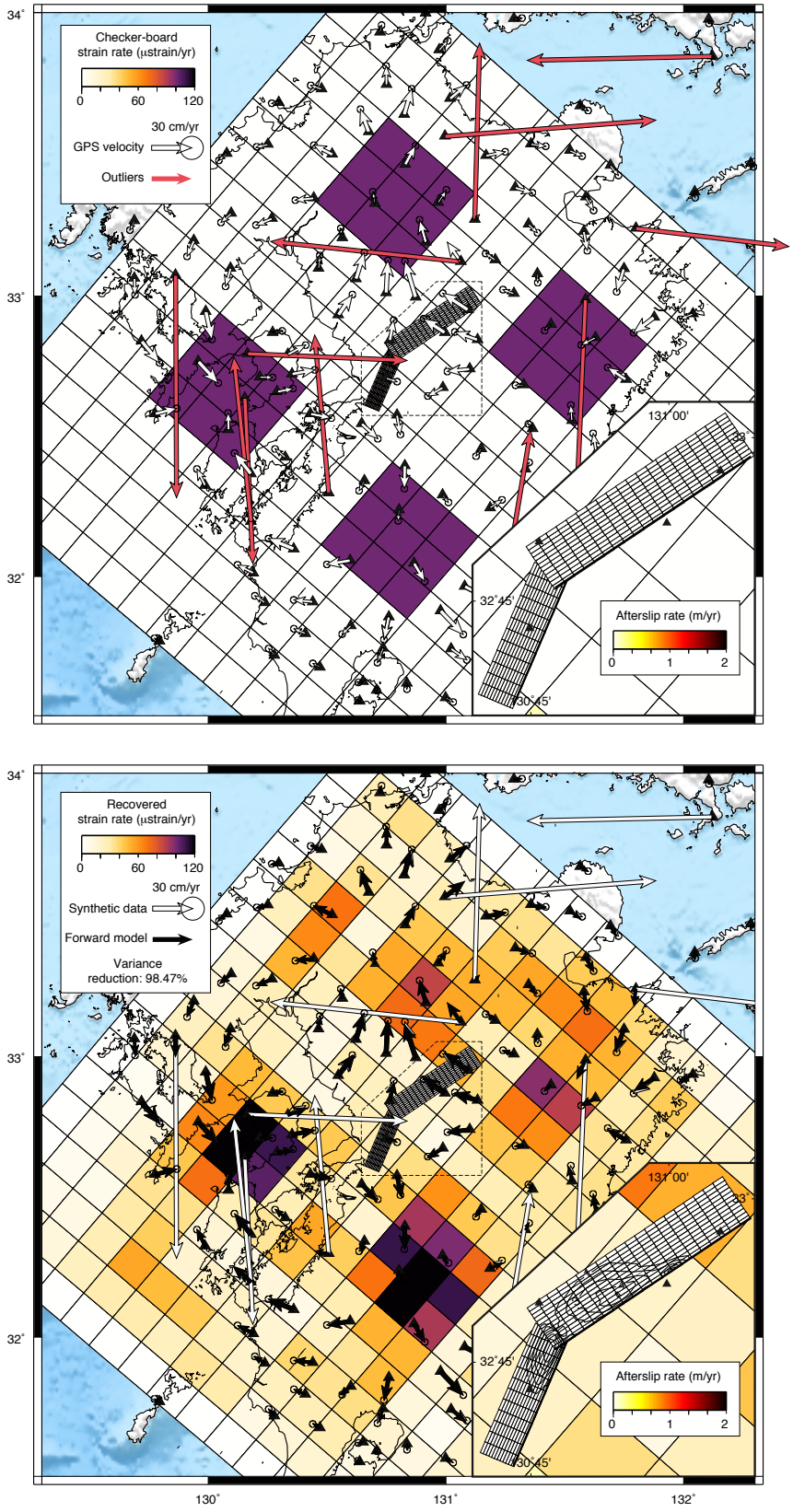


Figure S7: Checkerboard strain-rate test with outliers and outlier detection. Strain rates in the lower crustal strain volumes (20-40km) are shown in map view with afterslip rates on the fault and contours of coseismic slip (lower-right inset). GPS stations are indicated with black triangles. Upper pane shows strain-rate model set-up and calculated displacements with white arrows, outliers are included as red arrows. Lower pane shows recovered model and displacements in black arrows.

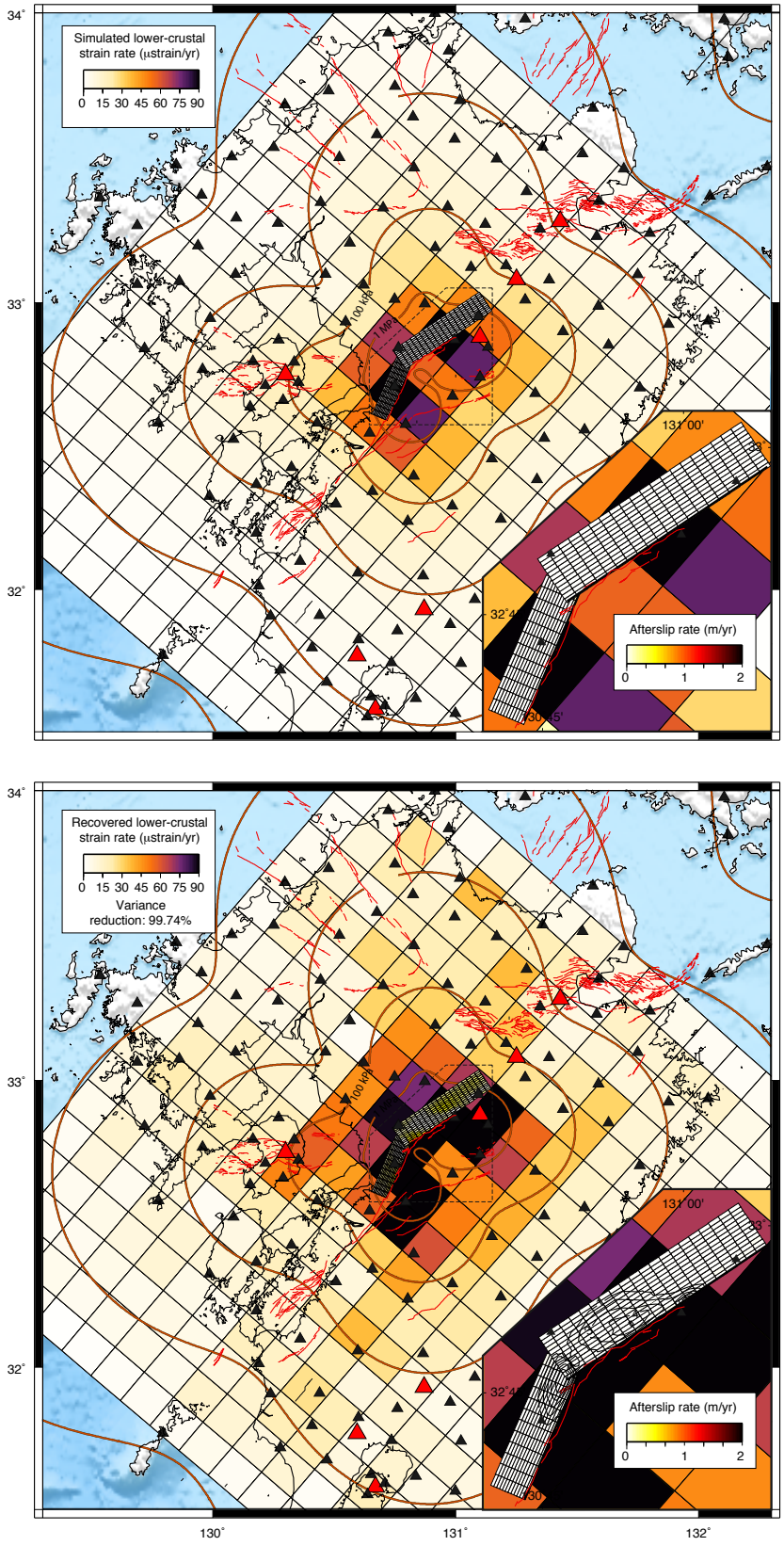


Figure S8: Uniform viscosity test with outliers and outlier detection. Strain rates in the lower crustal strain volumes (20-40km) are shown in map view with afterslip rates on the fault and contours of coseismic slip (lower-right inset). GPS stations are indicated with black triangles, known faults mapped with red lines, and volcanoes with red triangles. The upper panel shows the strain-rate model set-up and the lower panel shows recovered strain rates and slip rates.

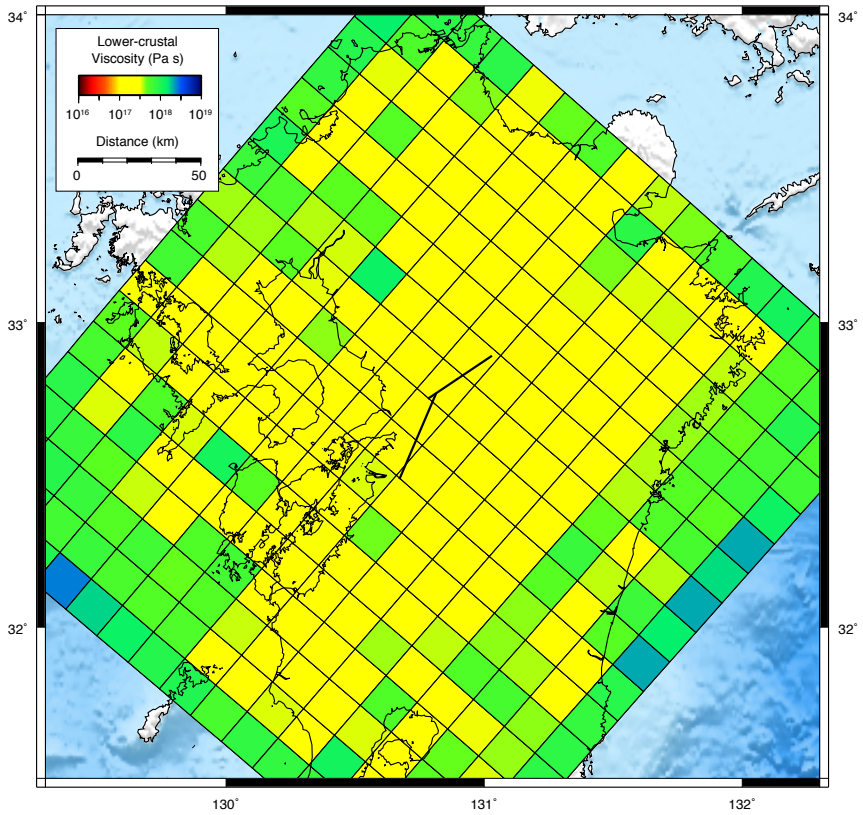


Figure S9: Uniform viscosity test with outliers and outlier detection. Recovered transient viscosity in the lower crustal strain volumes (20-40km) are shown in map view. Target transient viscosity is uniform $10^{17}$ Pa s with assumed steady-state uniform viscosity of $10^{19}$ Pa s.

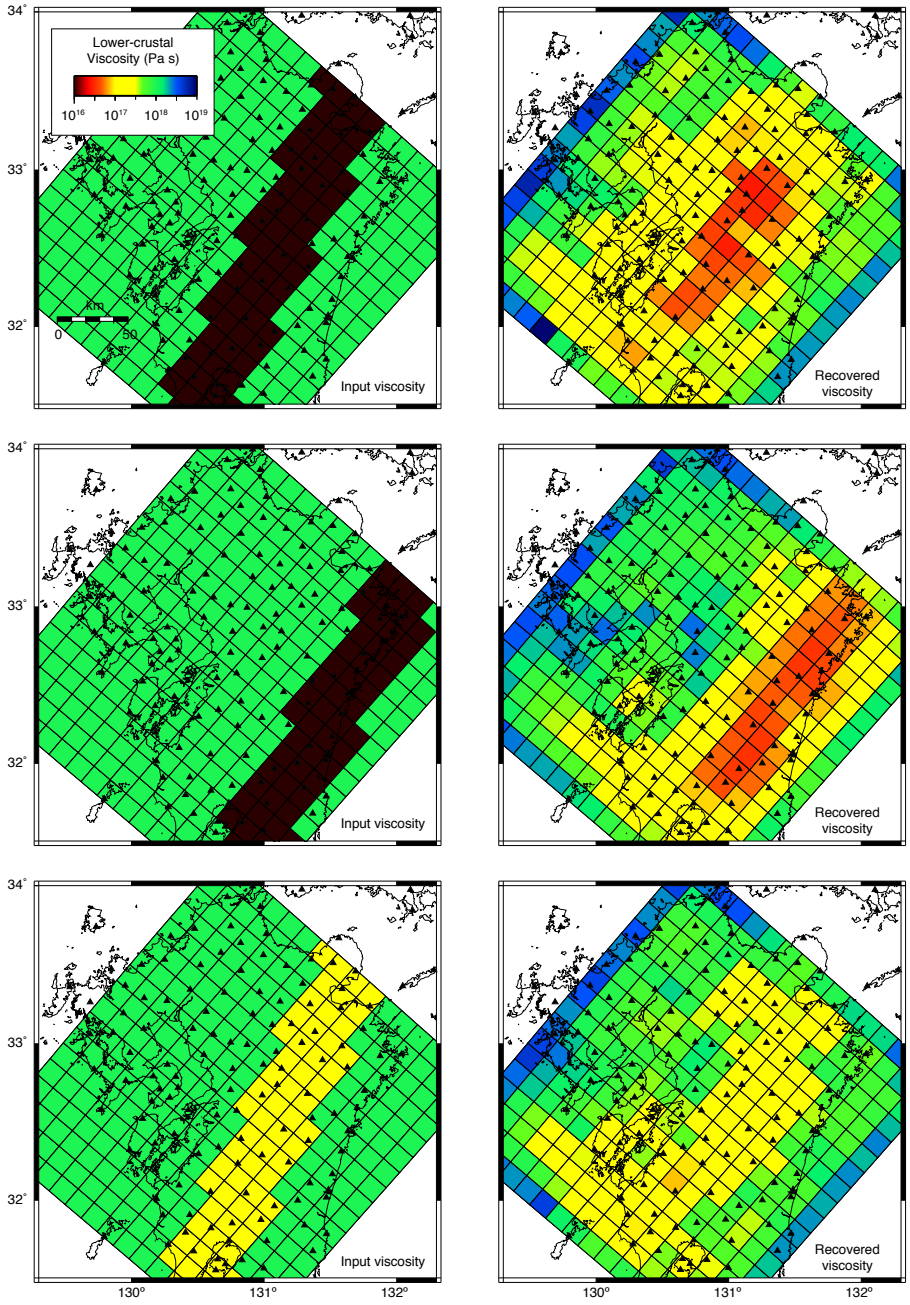


Figure S10: Spatially varying viscosity test with outliers and outlier detection. GPS stations are indicated with black triangles. The left panels show the viscosity model set-up and the right panels show recovered transient viscosity.

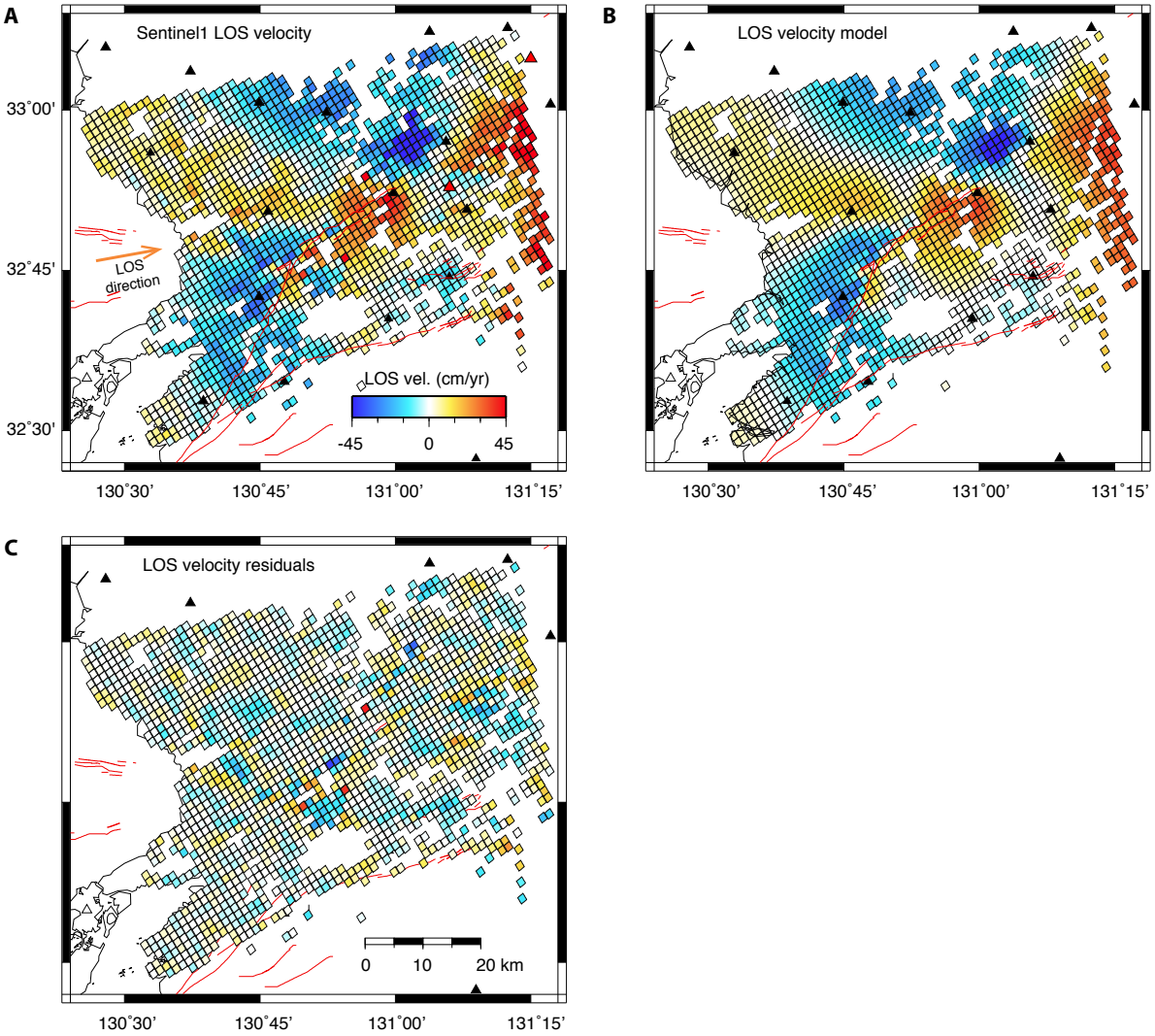


Figure S11: Observed and modelled line of sight InSAR postseismic deformation. A) Unwrapped Sentinel-1 line of sight (LOS) InSAR velocity composite from three acquisitions between 20th April 2016 and 7th June 2016. GPS stations are indicated with black triangles, known faults mapped with red lines, LOS vector in orange line, and volcanoes with red triangles. B) Line of sight postseismic velocity model, with contributions from afterslip and ductile flow in lower crustal strain volumes. The model captures the key features of the observations, excepting some high-frequency fluctuations, especially those following the fault traces of the Hinagu and Futagawa faults. C) Line of sight residuals, illustrating the high frequency fluctuations not captured in the postseismic velocity model, and otherwise negligible residual displacements.

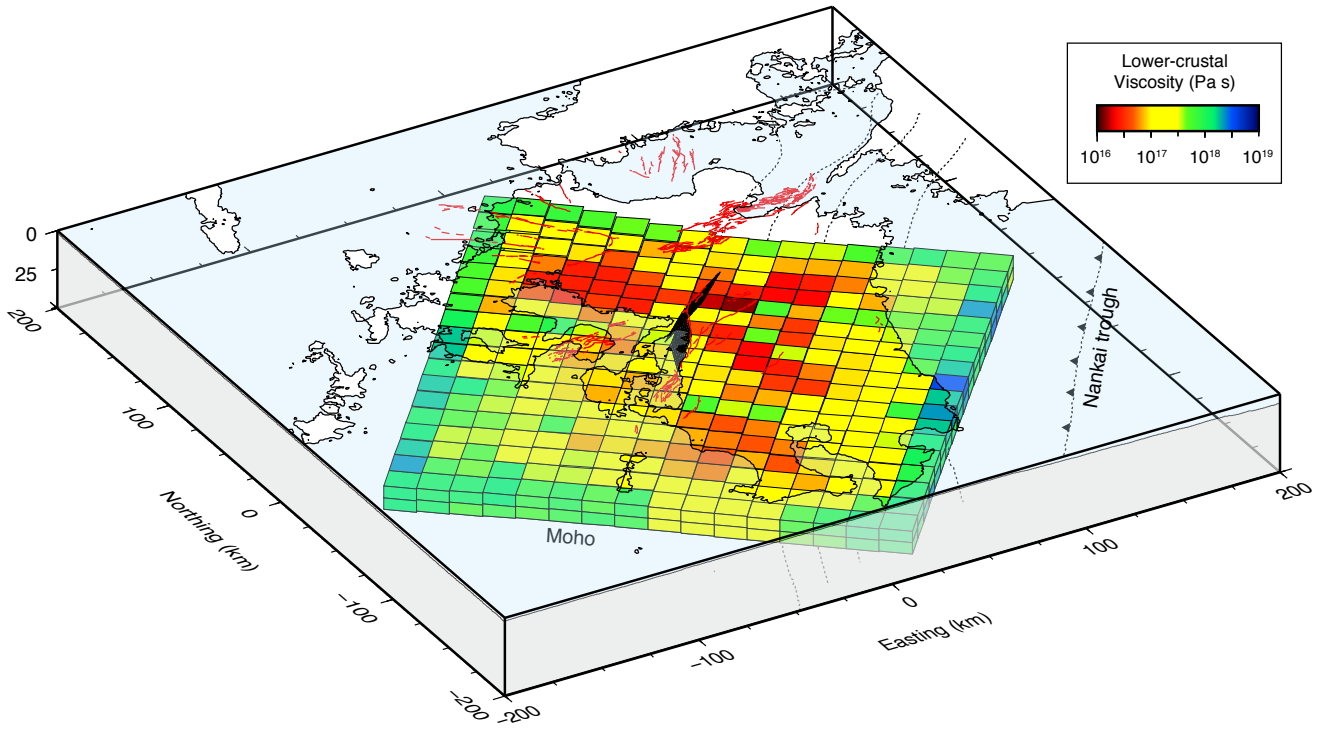


Figure S12: Transient viscosity of the lower crust illustrated in 3D with the Hinagu and Futagawa faults outlined in black and other fault surfaces traces shown in red. Downgoing Philippine Sea plate shown in dashed contours at 20km depth intervals.